

Airborne Measurements of Scale-Dependent Latent Heat Flux Impacted by Water Vapor and Vertical Velocity over Heterogeneous Land Surfaces During the CHEESEHEAD19 Campaign

Guo Lin¹, Zhien Wang¹, Yufei Chu¹, Conrad Ziegler², Xiao-Ming Hu³, Ming Xue³, Bart Geerts⁴, Sreenath Paleri⁵, Ankur Rashmikanth Desai⁵, Kang Yang¹, Min Deng⁶, and Jonathan DeGraw³

¹University of Colorado Boulder

²National Severe Storms Laboratory

³University of Oklahoma

⁴University of Wyoming

⁵University of Wisconsin-Madison

⁶Brookhaven National Laboratory

July 7, 2023

Abstract

The spatiotemporal variability of latent heat flux (LE) and water vapor mixing ratio (rv) variability are not well understood due to the scale-dependent and nonlinear atmospheric energy balance responses to land surface heterogeneity. Airborne in situ and profiling Raman lidar measurements with the wavelet technique are utilized to investigate scale-dependent relationships among LE, vertical velocity (w) variance (s2w), and rv variance (s2wv) over a heterogeneous surface in the Chequamegon Heterogeneous Ecosystem Energy-balance Study Enabled by a High-density Extensive Array of Detectors 2019 (CHEESEHEAD19) field campaign. Our findings reveal distinct scale distributions of LE, s2w, and s2wv at 100 m height, with a majority scale range of 120m-4km in LE, 32m-2km in s2w, and 200 m – 8 km in s2wv. The scales are classified into three scale ranges, the turbulent scale (8m-200m), large-eddy scale (200m-2km), and mesoscale (2 km-8km) to evaluate scale-resolved LE contributed by s2w and s2wv. In the large-eddy scale in Planetary Boundary Layer (PBL), 69-75% of total LE comes from 31-51% of the total sw and 39-59% of the total s2wv. Variations exist in LE, s2w, and s2wv, with a range of 1.7-11.1% of total values in monthly-mean variation, and 0.6-7.8% of total values in flight legs from July to September. These results confirm the dominant role of the large-eddy scale in the PBL in the vertical moisture transport from the surface to the PBL. This analysis complements published scale-dependent LE variations, which lack detailed scale-dependent vertical velocity and moisture information.

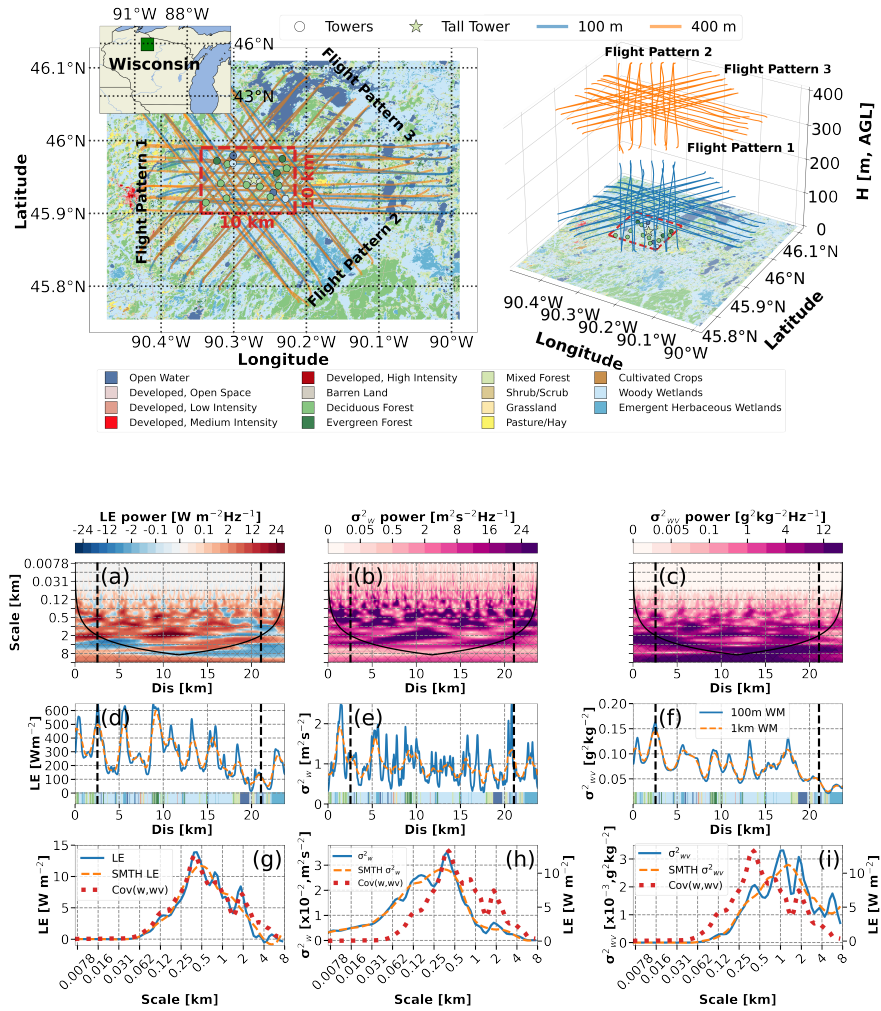
Hosted file

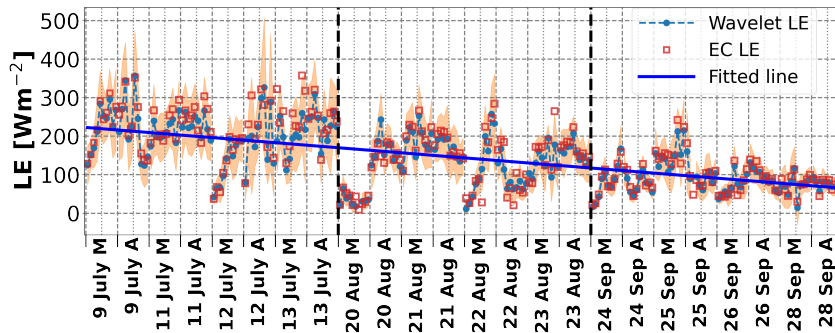
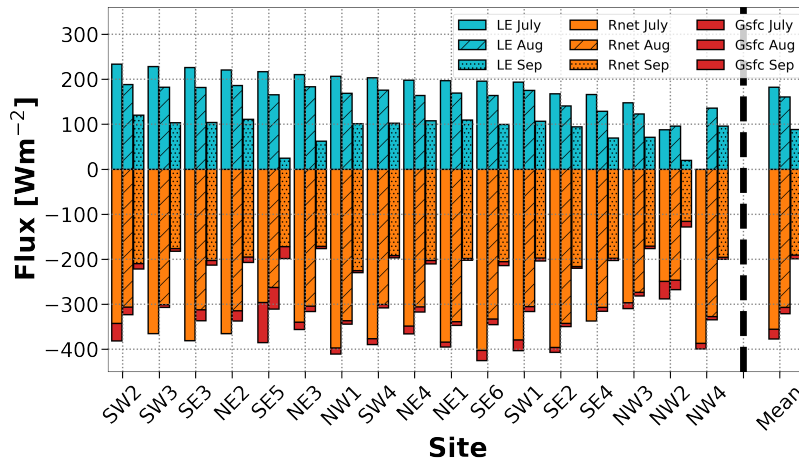
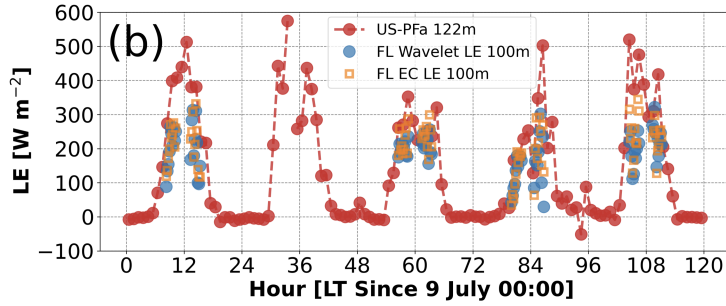
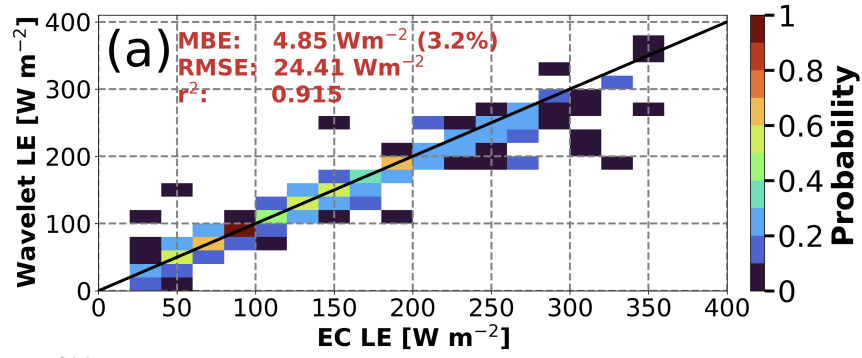
967818_0_art_file_11153792_rx8fs9.docx available at <https://authorea.com/users/636175/articles/653186-airborne-measurements-of-scale-dependent-latent-heat-flux-impacted-by-water-vapor-and-vertical-velocity-over-heterogeneous-land-surfaces-during-the-cheesehead19-campaign>

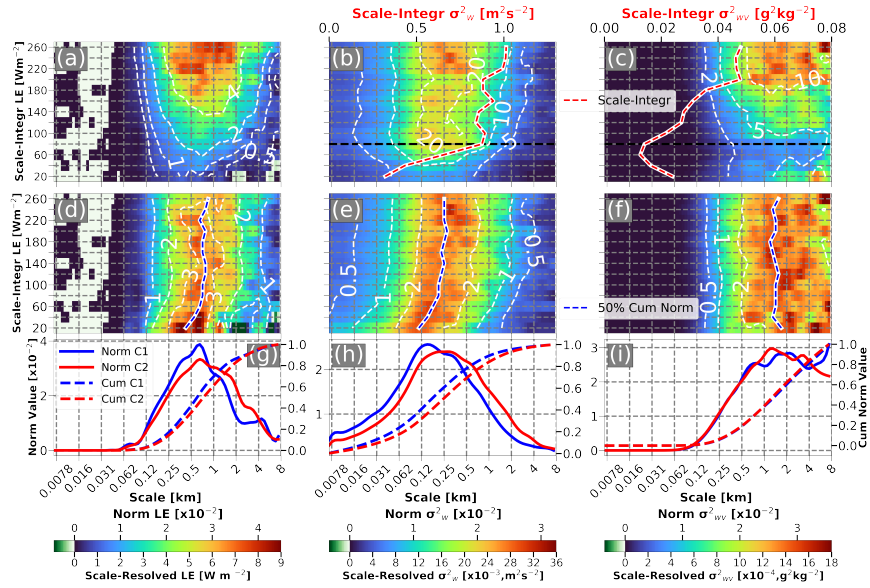
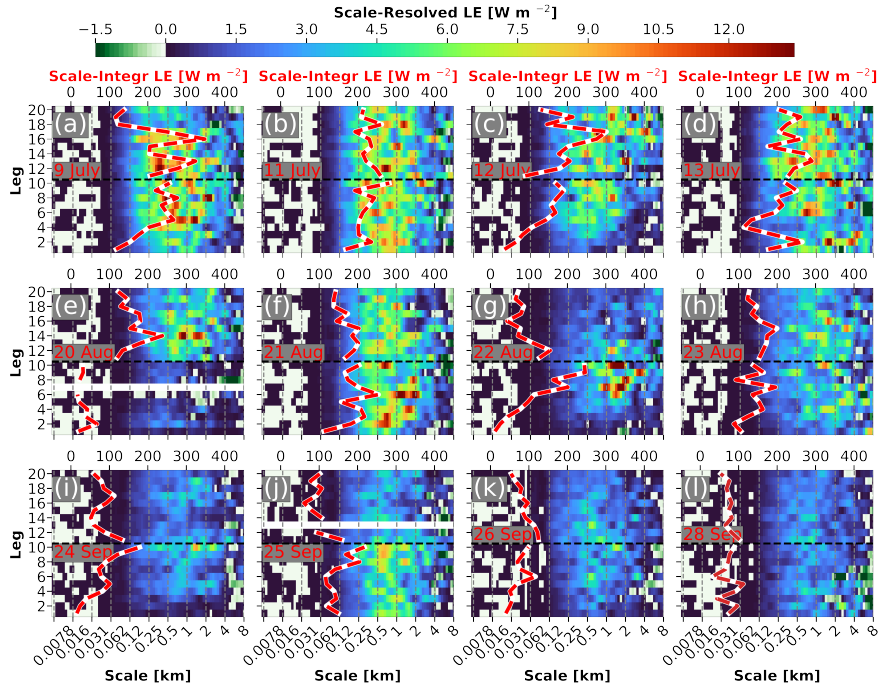
Hosted file

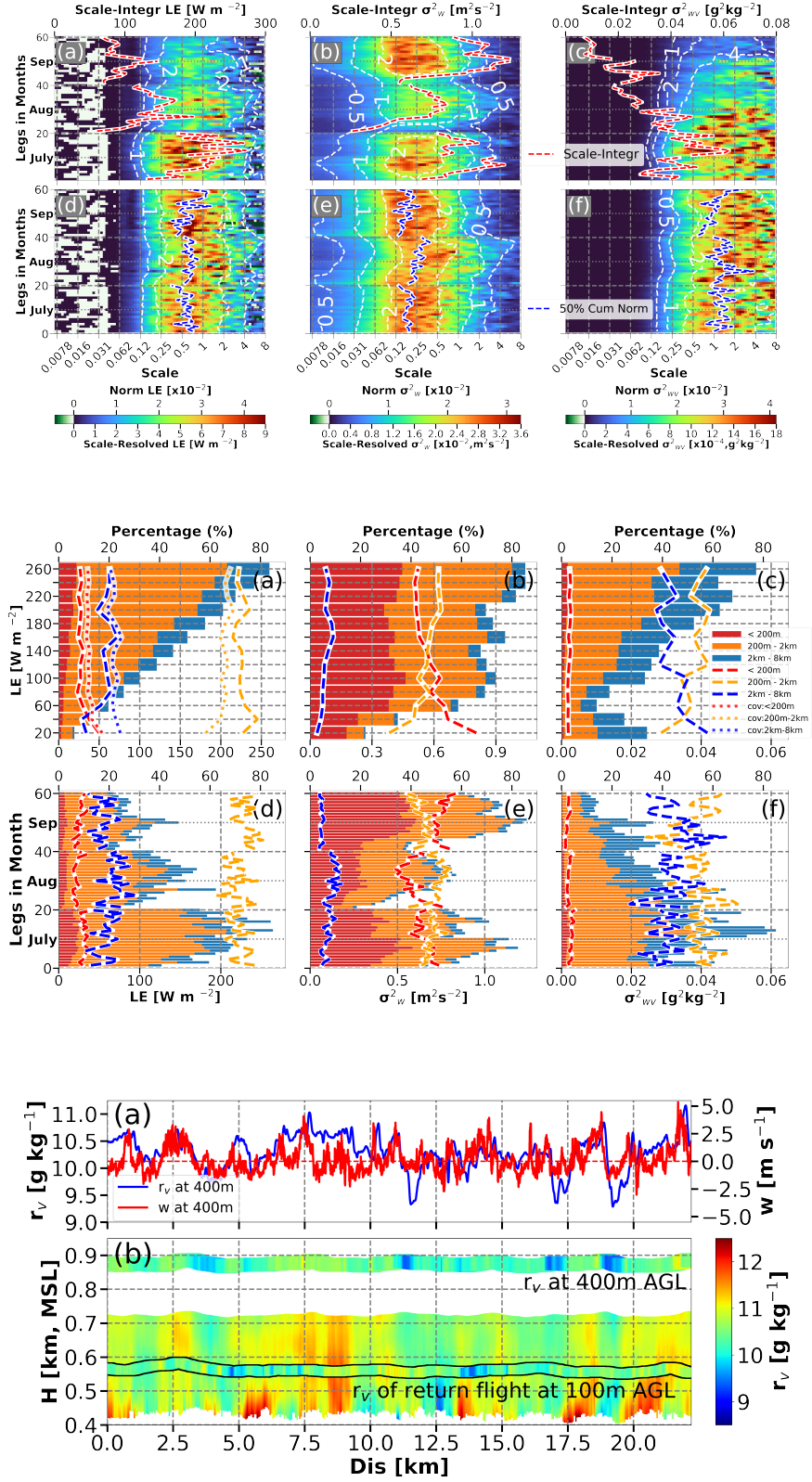
967818_0_supp_11153796_rx8fs9.docx available at <https://authorea.com/users/636175/articles/653186-airborne-measurements-of-scale-dependent-latent-heat-flux-impacted-by-water->

vapor-and-vertical-velocity-over-heterogeneous-land-surfaces-during-the-cheesehead19-campaign









1 **Airborne Measurements of Scale-Dependent Latent Heat Flux Impacted by Water Vapor**
2 **and Vertical Velocity over Heterogeneous Land Surfaces During the CHEESEHEAD19**
3 **Campaign**

4
5 Guo Lin^{1,2}, Zhien Wang^{1,2*}, Yufei Chu^{1,2}, Conrad Ziegler^{3,4}, Xiao-Ming Hu^{4,5}, Ming Xue^{4,5}, Bart
6 Geerts⁶, Sreenath Paleri⁷, Ankur R. Desai⁷, Kang Yang^{1,2}, Min Deng⁸, and Jonathan DeGraw^{4,5}

7
8 ¹*Department of Atmospheric and Oceanic Sciences, University of Colorado Boulder, Boulder, Colorado*

9 ²*Laboratory for Atmospheric and Space Physics, University of Colorado Boulder, CO*

10 ³*NOAA/National Severe Storms Laboratory, Norman, OK*

11 ⁴*School of Meteorology, University of Oklahoma, Norman, OK*

12 ⁵*Center for Analysis and Prediction of Storms, University of Oklahoma, Norman, OK*

13 ⁶*Department of Atmospheric Science, University of Wyoming, Laramie, WY*

14 ⁷*Department of Atmospheric and Oceanic Sciences, University of Wisconsin-Madison, Madison, WI*

15 ⁸*Environmental and Climate Sciences Department, Brookhaven National Laboratory, Upton, NY*

16
17 To be submitted to *JGR: Atmospheres*

18 Date: July 2023

19
20 *Corresponding author: Zhien Wang (Zhien.Wang@colorado.edu)

21 Laboratory for Atmospheric and Space Physics and Department of Atmospheric and Oceanic
22 Sciences, University of Colorado Boulder, 3665 Discovery Dr., Boulder, CO 80303.

23
24 **Key Points**

- 25
- 26 • The scale-dependent distribution of latent heat flux, vertical velocity variance, and water
vapor variance at 100 m over a heterogeneous surface is described.
 - 27 • In the large-eddy scale, 69 to 75 % of total latent heat flux is contributed by 32-45% of
28 total vertical velocity variance and 35-55 % of total water vapor variance.
 - 29 • The large-eddy scale contributes most of the vertical moisture transport from the surface
30 to the Planetary Boundary Layer.
- 31

Abstract

32
33
34 The spatiotemporal variability of latent heat flux (LE) and water vapor mixing ratio (r_v)
35 variability are not well understood due to the scale-dependent and nonlinear atmospheric energy
36 balance responses to land surface heterogeneity. Airborne in situ and profiling Raman lidar
37 measurements with the wavelet technique are utilized to investigate scale-dependent
38 relationships among LE, vertical velocity (w) variance (σ_w^2), and r_v variance (σ_{wv}^2) over a
39 heterogeneous surface in the Chequamegon Heterogeneous Ecosystem Energy-balance Study
40 Enabled by a High-density Extensive Array of Detectors 2019 (CHEESEHEAD19) field
41 campaign. Our findings reveal distinct scale distributions of LE, σ_w^2 , and σ_{wv}^2 at 100 m height,
42 with a majority scale range of 120 m-4 km in LE, 32 m - 2 km in σ_w^2 , and 200 m – 8 km in σ_{wv}^2 .
43 The scales are classified into three scale ranges, the turbulent scale (8 m – 200 m), large-eddy
44 scale (200 m–2 km), and mesoscale (2 km – 8 km) to evaluate scale-resolved LE contributed by
45 σ_w^2 and σ_{wv}^2 . In the large-eddy scale in Planetary Boundary Layer (PBL), 69-75% of total LE
46 comes from 31-51% of the total σ_w^2 and 39-59% of the total σ_{wv}^2 . Variations exist in LE, σ_w^2 , and
47 σ_{wv}^2 , with a range of 1.7-11.1% of total values in monthly-mean variation, and 0.6–7.8% of total
48 values in flight legs from July to September. These results confirm the dominant role of the
49 large-eddy scale in the PBL in the vertical moisture transport from the surface to the PBL. This
50 analysis complements published scale-dependent LE variations, which lack detailed scale-
51 dependent vertical velocity and moisture information.

52

Plain Language Summary

53
54
55
56
57
58
59
60
61
62
63
64
65
66
67

The vertical water vapor transport in the planetary boundary layer (PBL), and the associated latent heat flux (LE), are critical for the atmospheric hydrological cycle, radiation balance, and cloud formation. However, the vertical moisture transport varies nonlinearly at multiple scales due to the land surface heterogeneity across multiple properties. This study investigates the scale-resolved impact of water vapor and vertical velocity on LE, using data collected aboard an atmospheric research aircraft flying low above the surface in summer over northern Wisconsin during the CHEESEHEAD19 campaign. This study finds that LE and water vapor variance is largest at the large-eddy scale in PBL and at the mesoscale. In contrast, vertical velocity variance is primarily present in turbulent and large-eddy scales in PBL. This study confirms the significant role of the large-eddy scale in PBL in contributing to the majority of the vertical moisture transport from the surface to the PBL top. These findings provide better insight into the factors influencing LE at different scales.

68 **1. Introduction**

69

70 Water vapor and latent heat flux (LE) in the Planetary Boundary Layer (PBL) play critical roles
71 in atmospheric dynamics, the hydrological cycle, radiation balance, and conversion of latent heat
72 (Garratt, 1994; Pielke et al., 2003; Linné et al., 2006; Kiemle et al., 2007; Stevens & Bony, 2013;
73 Stull, 2015; Hu et al., 2023). Relevant processes include surface evapotranspiration, transport
74 and diffusion through the PBL, and cloud formation and dissipation (LeMone et al., 2019). The
75 PBL, where the mixing process by turbulent eddies at different scales plays a critical role,
76 transports water vapor from the surface to the free atmosphere. LE in the PBL is derived from
77 the surface, through evapotranspiration, modulated by the entrainment of air in the free
78 troposphere, and PBL circulation and evolution (Linné et al., 2006). However, the land surface
79 heterogeneity across multiple properties drives spatial variability of the vertical transport at
80 various scales in a nonlinear fashion (Raupach & Finnigan, 1995; Avissar & Schmidt, 1998;
81 Platis et al., 2017). Depending on the relative magnitude of the surface and entrainment fluxes,
82 the idealized water vapor flux profile within the well-mixed convective boundary layer (CBL)
83 either decreases or increases with height, in a linear fashion (Stull, 1988). Bange et al. (2002),
84 investigating heat fluxes using airborne flux measurements in the CBL, found linear profiles of
85 sensible heat flux but not LE. Water vapor and LE measurements are crucial to understanding
86 water vapor transport and its variability in PBL. Although the importance of water vapor is well
87 recognized, its spatial and temporal variability is still poorly characterized by observations,
88 making model validation difficult (Linné et al., 2006; Eder et al., 2015; Wolf et al., 2017; Bou-
89 Zeid et al., 2020; Mauder et al., 2020; Butterworth et al., 2021; Metzger et al., 2021). Accurate
90 accounting of land-atmosphere interactions is critical for improving the performance of
91 numerical weather and climate models.

92

93 Water vapor variability on scales comparable to the finest resolution of climate and weather
94 models is not yet well characterized and understood due to the atmospheric responses from
95 energy balance on land surface heterogeneity, despite its significant influence on the
96 development of cloud and precipitation processes (Sherwood et al., 2010; Wang et al., 2010).
97 The land surface is usually heterogeneous over a wide range of spatial scales due to variability in,
98 among other parameters, vegetation, terrain, soil texture and wetness, cloud cover, and urban

99 areas (Mahrt, 2000; Desai et al., 2005; Desai et al., 2022b). However, measurements at a single
100 location, such as eddy correlation flux towers, are often used to represent the properties of a
101 larger region. Individual point sensors may not be representative in complex terrain or in varied
102 vegetation (Bou-Zeid et al., 2020; Mauder et al., 2020; Butterworth et al., 2021).

103
104 While most horizontal humidity transport occurs through advection on large scales and is well
105 resolved in atmospheric models, vertical transport is dominated by turbulence on sub-grid scales
106 and must be parameterized (Kiemle et al., 2007). The vertical transport of water vapor generated
107 by surface forcings from the heterogeneous land surface at multiple scales leads to scale-
108 dependent atmospheric variability (Avisar & Schmidt, 1998). Water vapor is a complex natural
109 multiscale phenomenon that requires scale-based parameterizations because it is hard to resolve
110 all the relevant spatial information directly in numerical simulations or through observations
111 (Pressel et al., 2014). The lack of understanding of the small-scale dynamics of water vapor
112 throughout the PBL leads to strong limitations in predicting localized phenomena in weather
113 models (Couvreur et al., 2005; Steinfeld et al., 2007; Hill et al., 2008; Hill et al., 2011). As such,
114 the multiscale nature of water vapor has continued to defy a generalized approach or theory for
115 “characterizing” its impact on the PBL (Mahrt, 2000). Heat and moisture exchange
116 measurements between the land surface and the atmosphere are critical to understanding the
117 causes of variability in the PBL.

118
119 The eddy covariance (EC) technique is widely used to estimate the energy exchange between the
120 surface and the atmosphere at a single location: water vapor fluxes are estimated from the
121 covariance of the water vapor and vertical velocity perturbations (Aubinet et al., 2012). The
122 water vapor flux ($\text{g kg}^{-1}\text{m s}^{-1}$) is the covariance of w (m s^{-1}) and r_v (g kg^{-1}). This flux translates
123 into the LE (W m^{-2}) by multiplying the air density and the latent heat of water vaporization. The
124 LE is a valuable tool for monitoring changes in local sources and sinks of water vapor subjected
125 to local influences at a fixed station over an extended period. The EC technique suffers from
126 certain limitations in covering the full spectrum of the atmospheric transport (Finnigan et al.,
127 2003; Mauder et al., 2007). A sufficiently long averaging interval is required to minimize the
128 spectral loss in the low-frequency part. Non-local mesoscale eddies might either be
129 geographically fixed to a surface heterogeneity, or slowly moving in weak wind conditions

130 (Mahrt, 1998). Traditional EC calculation approaches are usually inadequate for capturing
131 mesoscale features associated with the surface heterogeneity (Foken et al., 2011; Charuchittipan
132 et al., 2014; Gao et al., 2016; Butterworth et al., 2021).

133
134 Spatial sampling coverage from micro- γ scale (<20m) to meso- β scale (up to 200 km) can be
135 provided by high-frequency instruments aboard aircraft flying in the surface layer. (the scale
136 classification is based on Orlanski, 1975; Mauder et al., 2007; Paleri et al., 2022). Aircraft can
137 fly a long distance to cover mesoscale eddies during one flight which is favorable for
138 investigating atmospheric mesoscale motions whereas ground-based systems passively detect
139 eddies brought by the mean wind (Mauder et al., 2007). The airborne measurement offers the
140 advantage of reduced measurement time and increased sampling compared to ground-based in
141 situ tower measurements (Desjardins et al., 1995). Recent projects with airborne flux
142 measurements include the Boreal Ecosystem-Atmosphere Study (BOREAS; Sellers et al., 1995),
143 the Northern Hemisphere Climate Processes Land-Surface Experiment (NOPEX; Halldin et al.,
144 1999), the Lindenberg Inhomogeneous Terrain – Fluxes between Atmosphere and Surface: a
145 Long-term Study (LITFASS-98; Beyrich et al., 2002) and LITFASS-2003 (Beyrich &
146 Mengelkamp, 2006), MAtter fluxes in Grasslands of Inner Mongolia as influenced by stocking
147 rate (MAGIM; Butterbach-Bahl et al., 2011), and ScaleX (Wolf et al., 2017). The airborne
148 estimation of LE is based on the combination of water vapor with vertical velocity measurements
149 using the EC technique (Linné et al., 2006) and wavelet technique (Mauder et al., 2007; Metzger
150 et al., 2013; Paleri et al., 2022). Mauder et al. (2007) found that the differences between these
151 techniques are relatively small, especially less than 2% for LE between the EC and wavelet
152 techniques. Differences between aircraft and tower-based estimates of water vapor fluxes are
153 often much larger (Desjardins et al. (1997). Aircraft can serve as extended observation platforms
154 for the scaling up from local (tower-based) to regional estimates of surface-atmosphere energy
155 exchange (Butterworth et al., 2021; Metzger et al., 2021). Although airborne measurements have
156 limitations in sampling duration, frequency, and distance due to operational considerations and
157 high costs (Desjardins et al., 1997; Mauder et al., 2007), the airborne EC measurements are
158 suitable for characterizing the water vapor and LE variability in a targeted experiment.

159

160 Here, we characterize the scale-dependence of LE, vertical velocity (w) variance (σ_w^2), and water
161 vapor (r_v) variance (σ_{wv}^2) at the 100 m above ground level (AGL) flight level in the
162 Chequamegon Heterogeneous Ecosystem Energy-Balance Study Enabled by a High-Density
163 Extensive Array of Detectors 2019 (CHEESEHEAD19) campaign (Butterworth et al. 2021). The
164 objective is to investigate the spatial-dominant scale of LE, σ_w^2 , and σ_{wv}^2 in the lower PBL and
165 how σ_w^2 and σ_{wv}^2 impact LE variability on diurnal to seasonal scales. Our study examines three
166 hypotheses on scaled-dependent LE, measured within the PBL during the daytime, based on the
167 literature discussed above:

168

169 **H1:** The spectral characteristics of σ_w^2 and σ_{wv}^2 are different.

170 **H2:** σ_w^2 generated by the surface is concentrated across scales less than the PBL height, which is
171 normally below 2 km.

172 **H3:** The scale-dependent σ_{wv}^2 includes the contributions of the entrainment of dry air from the
173 free troposphere, and PBL circulation and evolution, which are in large-eddy scale in PBL and
174 even mesoscale.

175

176 Ultimately, by contrasting the contributing spatial scales of the LE, σ_w^2 , and σ_{wv}^2 , this study
177 leads to a more accurate quantitative assessment of spatially localized contributions from all the
178 relevant transport scales. Section 2 introduces the CHEESEHEAD19 field campaign and reviews
179 the data collection methods, datasets, and instruments. The temporal and spatial variability of LE
180 and how σ_w^2 and σ_{wv}^2 impact are detailed in Section 3, while discussion and conclusions are
181 presented in Section 4 and Section 5.

182

183

184 **2. Data and Methodology**

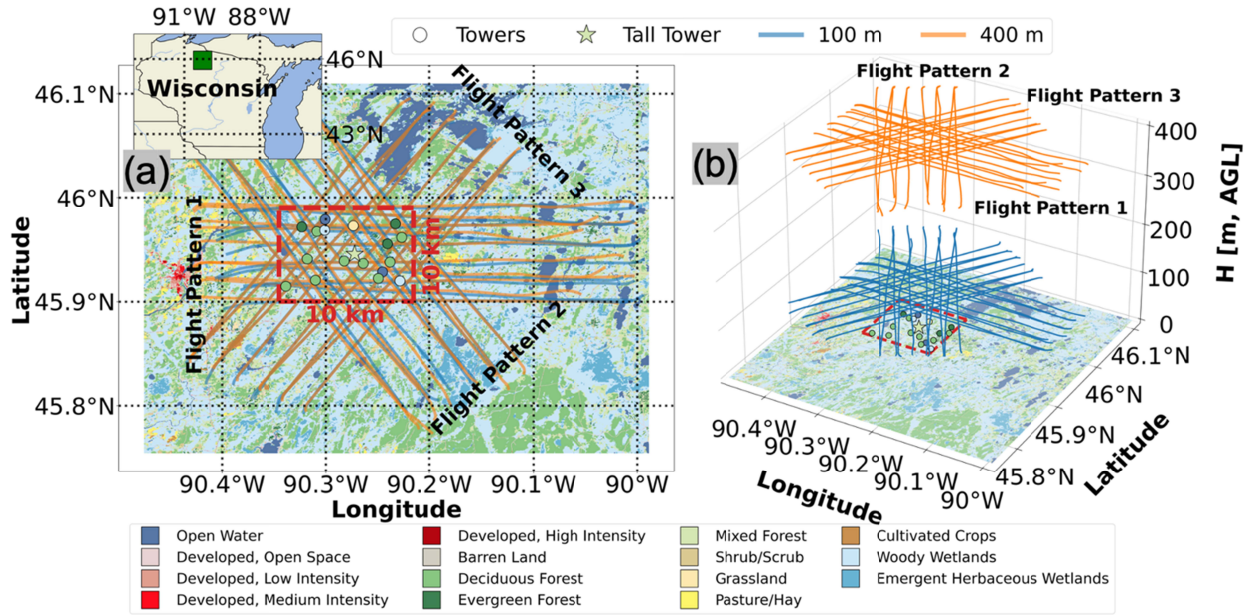
185

186 **2.1 Experimental Procedure**

187

188 The CHEESEHEAD19 was an intensive field campaign supported by the National Science
189 Foundation in the Chequamegon-Nicolet National Forest of Wisconsin from June to October
190 2019 (Butterworth et al., 2021). The experiment was designed to intensively sample land–surface
191 properties and the BL responses to surface properties across a heterogeneous mid-latitude
192 forested landscape. The land cover within the CHEESEHEAD19 domain is dominated by
193 conifers, deciduous forest, mixed forest, wetlands, and open water, according to the National
194 Land Cover Database (NLCD) 2019 land cover (Figure 1; Dewitz & U.S. Geological Survey,
195 2021). The canopy heights range from 0 to 35 meters, leading to a horizontally heterogeneous
196 surface. This forest, with diverse surface properties varying at multiple scales, was selected to
197 address a crucial gap in our current understanding of surface atmospheric exchanges over a
198 heterogeneous flat land surface (Bou-Zeid et al., 2020). Measurements of CHEESEHEAD used a
199 suite of observing platforms over a core 10 x 10 km² domain (the red dashed domain in Figure 1a)
200 and a 30 km x 30 km extended domain for airborne measurements. The study domain was partly
201 chosen due to the history of atmospheric science research in the region (Davis et al., 2003; Desai
202 et al., 2022a). The EC tower network consisted of 17 flux towers from the National Center for
203 Atmospheric Research (NCAR) - Integrated Surface Flux Station (ISFS) network (colored
204 circles in Figure 1), two additional contributed towers in grassland and a lake, and the tall
205 Department of Energy Ameriflux regional tower (US Pfa/WLEF; the star in Figure 1) (Desai,
206 2023). A majority of the ISFS sites had flux instruments mounted at 33 m AGL for forests while
207 instruments for wetland, grass, and lake sites were mounted between 1 and 3 m AGL to maintain
208 consistent sampling within homogenous flux footprints (Oncley, 2021). The US PFA tower has
209 sampled greenhouse gas profiles, meteorological data, and EC flux measurements (energy,
210 carbon, momentum) at 30, 122, and 396 m above ground level (AGL) since 1995 (Berger et al.,
211 2001; Davis et al., 2003). The fluxes can be simultaneously measured at seventeen points with
212 tower-based systems and short periods with airborne measurements during Intensive Observation
213 Periods (referred to as IOPs henceforth). Thus, the temporal and spatial characteristics of
214 ground-based and airborne measurements complement each other to evaluate land-atmosphere

215 interactions in PBL at the site and regional scales (Butterworth et al., 2021; Hu et al., 2021;
 216 Paleri et al., 2022).
 217



218
 219 **Figure 1.** (a) Location of the CHEESEHEAD19 domain (blue square) in Wisconsin (insert map)
 220 and colored land classification map from the NLCD 2019 of the area around the
 221 CHEESEHEAD19 domain with three distinct University of Wyoming King Air (UWKA) flight
 222 patterns at 100 m (blue lines) and 400 m (orange lines); (b) 3D map showing the three UWKA
 223 flight patterns at 100 m (blue lines) and 400 m (orange lines). The red dashed square represents
 224 the study domain of flux towers, and the dots and a star indicate the flux tower locations colored
 225 by their land cover types.

226

227 2.2 Airborne Observations

228

229 The airborne observations aimed to examine PBL responding to spatial heterogeneous land cover.
 230 The University of Wyoming King Air (UWKA) aircraft was equipped a suite of atmospheric
 231 measurement probes, including wind, temperature, and humidity measurements up to 25 Hz to
 232 estimate turbulent fluxes (French et al., 2021). The UWKA used a high-precision geo-
 233 positioning system (Trimble/Appianix, model POS AV410) and gust probe to obtain 3D position
 234 and 3D velocity information, including horizontal wind speed (W_{spd}), horizontal wind direction

235 ($Wdir$), and w used in this study (Haimov & Rodi, 2013). The r_v is measured by LI-COR LI-7000
 236 CO₂/H₂O analyzer. The sampling frequency of w and r_v is 25 Hz, and the aircraft flew at a true
 237 air speed of ~ 90 m/s. Net radiation ($Rnet$) data were also collected to provide information on
 238 theoretical maximum latent plus sensible heat fluxes. The UWKA also sampled 2D vertical
 239 profiles of water vapor, aerosols, and temperature below the flight level using a nadir-pointing
 240 Compact Raman Lidar (CRL; Liu et al., 2014; Wu et al., 2016; Lin et al., 2019; Lin et al., 2023)
 241 and aerosols with the zenith-pointing Wyoming Cloud Lidar (Wang et al., 2009; Lin et al., 2021)
 242 at 400 m height. Three IOPs with the UWKA were conducted during the experiment in each
 243 month from July to September (details in Table 1). The flight consisted of two 3-h flights for
 244 each research flight (RF in Table 1), one in the morning (1400–1700 UTC; odd numbers in RF,
 245 using M as morning) and another in the afternoon (1900–2200 UTC; even numbers in RF, using
 246 A as afternoon). The flight times relative to sunrise and sunset differ in RFs and months (Table
 247 1). Three flight patterns (FPs) were conducted in IOPs (oriented W–E for FP1; NW-SE for FP2,
 248 SW–NE for FP3 in Figure 1 and Table 1) based on a flux heterogeneity optimization approach
 249 (Metzger et al., 2021).

250

251 **Table 1.** IOPs, dates (The M represents morning and A represents afternoon), RF numbers and
 252 times, sunrise and sunset times, flight patterns, flight-level winds, and net radiation of all
 253 IOPs.

IOP (#)	Date	Flight (#)	Time Period (Mor, UTC)	Time Period (Aft, UTC)	Sunrise (UTC)	Sunset (UTC)	Fight Pattern	Wspd (ms ⁻¹)	Wdir (deg)	Rnet (Wm ⁻²)
	9 July	M RF 01	1413 – 1616		1121		FP1	6.4	278	495
	9 July	A RF 02		1919 – 2119		2646	FP1	4.6	271	540
	11 July	M RF 03	1429 – 1635		1122		FP1	2.9	102	658
IOP	11 July	A RF 04		1922 – 2127		2644	FP1	6.0	319	633
01	12 July	M RF 05	1358 – 1606		1123		FP1	6.0	318	539
	12 July	A RF 06		1841 – 2045		2644	FP1	6.2	347	528
	13 July	M RF 07	1428 – 1631		1124		FP2	5.1	44	626
	13 July	A RF 08		1917 – 2115		2643	FP3	3.7	71	648
	20 Aug	M RF 09	1358 – 1611		1206		FP2	6.2	262	164
	20 Aug	A RF 10		1931 – 2150		2556	FP2	3.0	150	502
	21 Aug	M RF 11	1415 – 1635		1207		FP3	4.7	40	524
IOP	21 Aug	A RF 12		1918 – 2137		2555	FP3	6.0	49	479
02	22 Aug	M RF 13	1417 – 1639		1208		FP3	2.6	134	320
	22 Aug	A RF 14		1921 – 2146		2553	FP3	4.4	116	274
	23 Aug	M RF 15	1414 – 1637		1209		FP1	3.4	159	509
	23 Aug	A RF 16		1925 – 2145		2551	FP1	4.3	184	536

	24 Sep M	RF 17	1359 – 1635	1247		FP2	6.4	260	356
	24 Sep A	RF 18		1919 – 2139	2452	FP2	6.9	280	244
	25 Sep M	RF 19	1448 – 1708	1248		FP3	7.6	8	433
IOP	25 Sep A	RF 20		1936 – 2152	2450	FP3	9.2	343	159
03	26 Sep M	RF 21	1413 – 1634	1250		FP2	4.4	278	359
	26 Sep A	RF 22		1852 – 2114	2448	FP2	7.2	338	314
	28 Sep M	RF 23	1444 – 1705	1252		FP1	3.2	104	464
	28 Sep A	RF 24		1915 – 2134	2444	FP1	4.0	107	349

254

255 During the UWKA RFs, the aircraft flew a ~30 km leg at 400 m AGL (orange flight tracks in
 256 Figure 1) to sample the temperature, aerosols, and moisture profiles of the PBL with the CRL.
 257 The UWKA then flew a ~30 km leg back at 100 m AGL (orange flight tracks in Figure 1) to
 258 measure turbulent fluxes at flight level. The 400 m and 100 m flights were repeated ten times in
 259 every RF. The 100 m altitude is the lowest altitude deemed safe to fly within the surface layer as
 260 the canopy height extends to 35m. The choice of FP was based on the prevailing wind direction:
 261 the one closest perpendicular to the prevailing wind was chosen (Metzger et al., 2021). The flight
 262 legs extended an average of 10 km beyond the core domain to maximize data coverage under
 263 different wind conditions and the number of independent atmospheric eddies observed by the
 264 aircraft EC measurements. The 30 km flight legs captured enough eddies and mesoscale
 265 variation to properly compute eddy correlation statistics for fluxes using the wavelet
 266 decomposition method (Mauder et al., 2007; Paleri et al., 2022). Although the CHEESEHEAD19
 267 dataset provided good spatial coverage but with limited temporal coverage (72 flight hours in 12
 268 days, all with fair-weather conditions), it is still one of the largest airborne flux measurement
 269 datasets collected to date.

270

271 **2.3 Wavelet Flux Analysis**

272

273 A wavelet transform can be used to evaluate the scale-dependent contribution of atmospheric
 274 fluxes from aircraft measurements (Attié & Durand, 2003; Strunin & Hiyama, 2005; Mauder et
 275 al., 2007; Vadrevu & Choi, 2011; Paleri et al., 2022). The wavelet functions and analysis
 276 methods were developed for time-frequency analysis revealing localized information (Farge,
 277 1992; Thomas & Foken, 2004). The wavelet analysis is a powerful mathematical tool that, based
 278 on the ergodic hypothesis, does not require data to be stationary at many different frequencies
 279 (Torrence & Compo, 1998; Strunin & Hiyama, 2005; Mauder et al., 2007), unlike other

280 conventional methods such as a Fourier transform (Foken & Wichura, 1996). In this regard, the
281 wavelet analysis is particularly suitable for aircraft data measured above heterogeneous terrain to
282 calculate atmospheric fluxes on different scales during the CHEESEHEAD19 field campaign.
283 The existing wavelet methodology is expanded to facilitate space-scale analysis of the UWKA
284 in-situ data from Torrence and Compo (1998) and (Mauder et al., 2007). The Morlet wavelet has
285 been selected as the mother wavelet in the field of atmospheric turbulent studies, because of its
286 good localization in space and frequency domains (e.g., Torrence & Compo, 1998; Mauder et al.,
287 2007; Paleri et al., 2022). The wavelet equations of the wavelet power spectrum, variance, power
288 co-spectrum, and covariance are described in detail in the Supplement. The wavelet spectrum
289 and co-spectrum depend on the scale-dependent bin size, but variance (Equation S7) and
290 covariance (Equation S11) are independent of bin size, since they are normalized by bin size.
291 Mauder et al. (2007) show examples of covariance calculated by the wavelet technique from
292 airborne in situ measurements and scale-resolved distributions in their Figure 4. In this study, the
293 wavelet technique is used to calculate and evaluate the 100 m flight-level scale-resolved
294 distribution and temporal variation of LE, σ_w^2 , and σ_w^2 for all flight legs from the July, August,
295 and September IOPs (Table 1). The normalized scale-resolved LE, σ_w^2 , and σ_w^2 calculated by
296 Equations S10 and S12 are used to analyze the relative scale-dependent contribution from σ_w^2
297 and σ_w^2 to LE regardless of their values.

298

299 **2.3.1 Example of Wavelet Variance and Covariance**

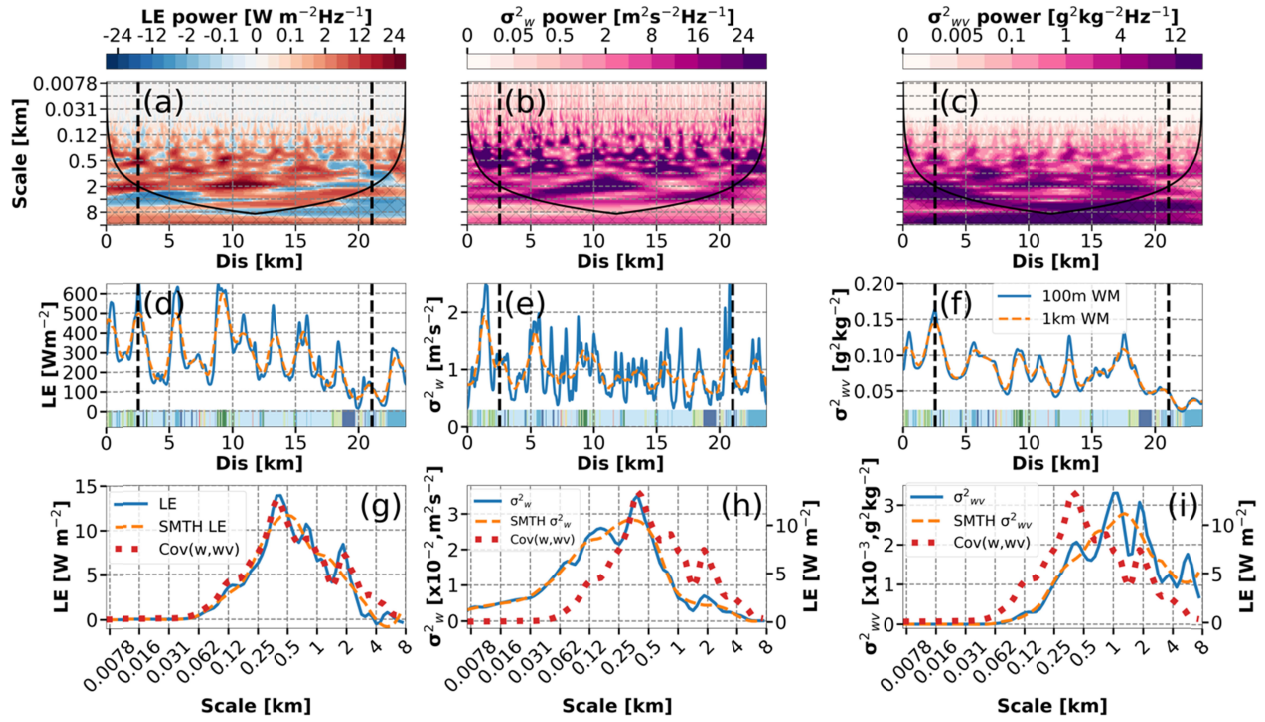
300

301 The wavelet method permits to allocate the information about flux contributions from the entire
302 flight track to a specific subsegment of that track. We apply wavelet calculation to the same
303 flight track of Figure 3 in Paleri et al. (2022) for comparison and to ensure consistent calculation
304 (Figure 2). The wavelet analysis is applied to calculate the wavelet power co-spectrum of LE,
305 and the wavelet power spectra of w and r_v (Figures 2a-c). We also calculated LE using Equation
306 S11, and σ_w^2 (m^2s^{-2}) and σ_{wv}^2 ($\text{g}^2 \text{kg}^{-2}$) using Equation S7 with 100 m flight-level data for spatial
307 and scale analysis (Figures 2d-i). The hashed areas shown in Figures 2a-c are the cone of
308 influence (COI) where edge effects due to discontinuities at the endpoints become important.
309 Since the wavelet decomposition deals with finite-length flight leg, errors will occur at the
310 beginning and end of the wavelet power spectrum (Torrence & Compo, 1998).

311
 312 Spatial variations of LE, σ_w^2 , and σ_{wv}^2 were calculated by normalizing power spectra and the co-
 313 spectrum with scale-dependent bin size and integrating the scale up to 8 km along the flight-track
 314 segment (Figures 2d-f) since the integrated processes covering the full-range scale may introduce
 315 uncertainties by the COI. The spatial LE, σ_w^2 , and σ_{wv}^2 are smoothed by 28-point average
 316 windows (100m; blue lines), and 278-point averaged windows (1km; orange lines in Figure 2d-f).
 317 The 1 km window-averaged LE varies from 60 to 600 Wm^{-2} in a 28 km flight track. The land
 318 classification is mapped out at the bottom of Figures 2d-f. The spatial LE is related to surface
 319 heterogeneity, with the lowest LE occurring at 18 km over water along the flight track. The
 320 maximum 600 Wm^{-2} latent heat flux at 9 km coincides with the cross-scalogram of LE power
 321 contribution up to 4 km (Figure 2a). However, the high value of LE does not correlate to only
 322 high σ_w^2 or high σ_{wv}^2 , but instead to the covariance of σ_w^2 and σ_{wv}^2 . The 600 Wm^{-2} LE at around
 323 9 km is collocated with 1.3 m^2s^{-2} σ_w^2 and 0.12 g^2kg^{-2} σ_{wv}^2 . Neither σ_w^2 nor σ_{wv}^2 is the maximum
 324 value in the segment.

325
 326 The spatial variations (Figure 2d-f) along the flight-track segment cannot resolve the scale
 327 contribution of σ_w^2 and σ_{wv}^2 to LE clearly. The leg-averaged scale-resolved LE (Figure 2g)
 328 reflects the importance of small-scale contributions with values greater than 2 Wm^{-2} in scales
 329 from 100 m to 3 km with a maximum LE of 14 Wm^{-2} at ~0.4 km. The scale-resolved σ_w^2 with
 330 values greater than $5 \times 10^{-2} \text{m}^2\text{s}^{-2}$ is between 16 m and 1.5 km within PBL turbulence scales (< 2
 331 km; Figure 2b). The scale-resolved σ_{wv}^2 is concentrated between 200 m and 8 km with a peak of
 332 $3.2 \times 10^{-2} \text{g}^2\text{kg}^{-2}$ at 1 km. The distribution of scale-resolved σ_{wv}^2 between 200 m and 8 km could
 333 result from large-eddy circulations in PBL and mesoscale forcings. To see the scale-resolved σ_w^2
 334 and σ_{wv}^2 contributing to the scale-resolved LE, the scale-resolved covariance between w' and r_v'
 335 ($\text{cov}_{(w,wv)}$) is calculated using Equation S13. The $\text{cov}_{(w,wv)}$ is shown in Figures 2g-i to compare the
 336 different scale-resolved distributions among LE, σ_w^2 , and σ_{wv}^2 .

337



338

339 **Figure 2.** A sample wavelet cross-scalogram between w and r_v in the result of (a) LE power; the
 340 wavelet scalogram of (b) σ_w^2 power and (c) σ_{wv}^2 power illustrating the scale-resolved spatial
 341 contributions along RF02 flight leg 2 at 100m AGL. The (d) scale-integrated LE, (e) σ_w^2 , and (f)
 342 σ_{wv}^2 along the flight tracks are calculated by integrating scalogram in spatial scales along the y-
 343 axis of panels a, b, and c, respectively. The (g) scale-dependent LE, (h) σ_w^2 and (i) σ_{wv}^2 are
 344 averaged over the flight leg between $2.5 \text{ km} < x < 21 \text{ km}$ (within two vertical black lines shown
 345 in panels a-f). Hashed portions in (a-c) below the black line represent the COI of edge effects.
 346 The vertical black lines represent the threshold of 2km influenced by COI for the chosen flight
 347 segment to calculate scale-dependent LE, σ_w^2 , and σ_{wv}^2 . The colored land classification map
 348 along the flight track is shown at the bottom of (d)-(f).

349

350 2.3.2 Wavelet and Eddy Covariance LEs Comparison

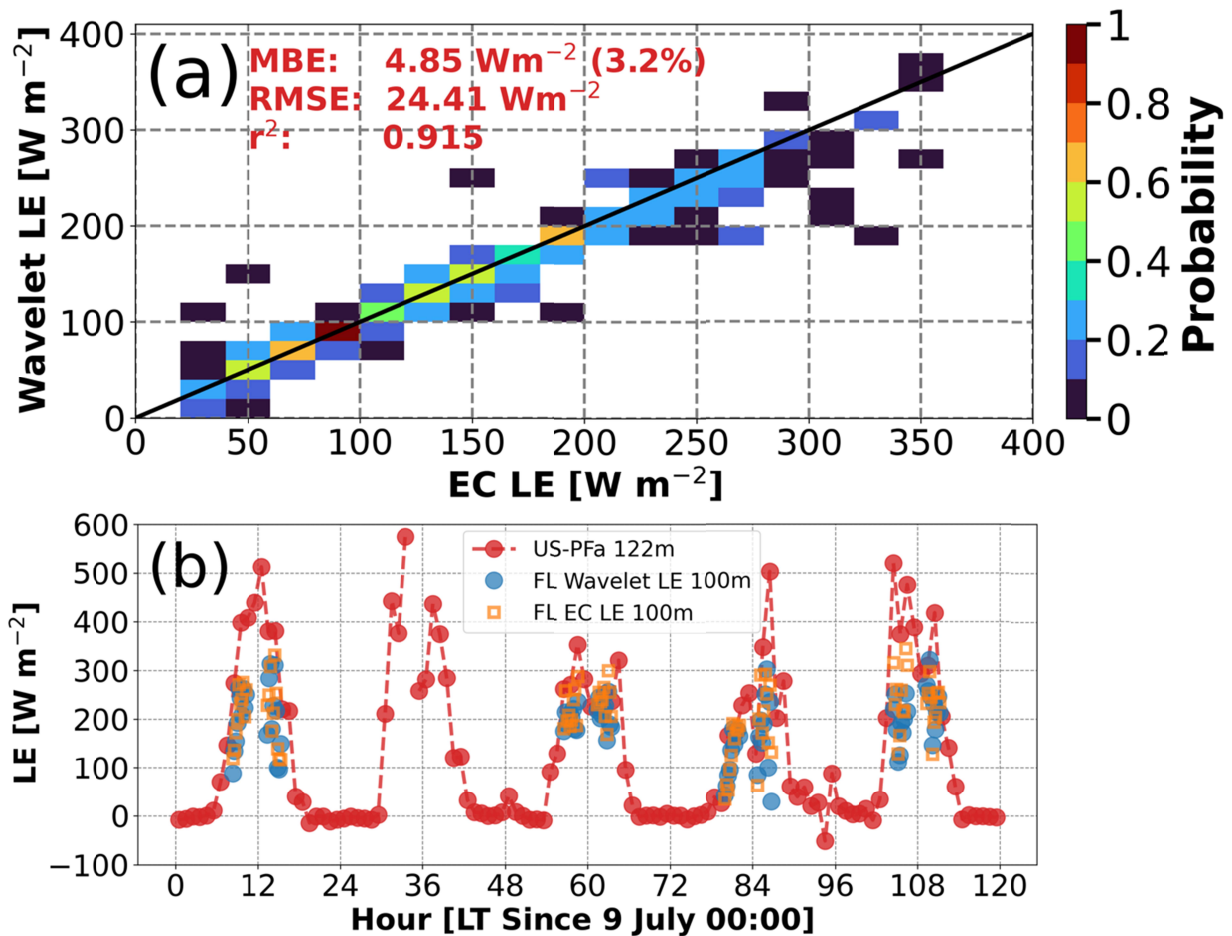
351

352 To examine the accuracy of wavelet-calculated airborne LEs at 100 m, the flight-leg averaged
 353 LEs of 240 flight legs calculated by the wavelet technique are compared with leg-averaged LEs
 354 from the traditional EC technique (Figure 3a). Since the influence of edge effects by COI is
 355 generally larger towards the ends of the wavelet cross-scalogram (Figure 2a), a threshold of
 356 chosen segment legs is in the scale of COI greater than 2 km to ensure a long-enough flight leg to

357 sample mesoscale eddies and to reduce significant edge effects from discontinuities at the
 358 endpoints for wavelet LE calculations (i.e., the flight segment between two vertical black lines in
 359 Figure 2a). The traditional leg-averaged EC LE is defined (Stull, 1988):

$$EC\ LE = \overline{w'r'_v} \quad (1)$$

360 where w' and r'_v are the w perturbation and r_v perturbation from leg-averaged values,
 361 respectively. The same flight segment is used for LE calculations with the two techniques. The
 362 2D histogram comparing traditional leg-averaged EC LEs against wavelet LEs for the 240 flight
 363 legs, shown in Figure 3a, has a bin size of $20\ Wm^{-2}$ from 0 to $400\ Wm^{-2}$. The wavelet LE is
 364 slightly smaller than the EC LE with a mean bias error (MBE) of $4.85\ Wm^{-2}$, $\sim 3.2\%$ of the total
 365 mean EC LE, and the root mean square error (RMSE) of $30\ Wm^{-2}$. The correlation coefficient (r^2)
 366 is 0.915. The low mean differences and high r^2 indicate reliable leg-averaged wavelet LE
 367 compared to the EC LE.
 368



369

370 **Figure 3.** (a) Comparison of airborne flight-level LEs calculated by the EC technique and the
371 wavelet technique for all 100 m flight legs during all three IOPs (Table 1) ; (b) comparison of
372 leg-averaged LEs at 100m flight level and LE at 122 m on the US PFa tall tower for the July IOP.
373 The flight-level LE is calculated by the wavelet technique (blue circles) and EC technique
374 (orange squares); The tall-tower LE is calculated by the EC technique.

375

376 To further evaluate the airborne wavelet LEs, the flight-level wavelet LEs and EC LEs at 100m
377 and the EC LEs of tall-tower US-PFa at 122m are compared (Figure 3b). The comparison of LE
378 is only in July because the tall towers measured inaccurate negative EC LEs at 122 m height
379 during the August IOP, while EC LEs at 30 m and 396 m were positive. The EC LEs in August
380 and September have been excluded from the quality control process. The airborne wavelet-
381 calculated LEs compare reasonably well with the airborne EC LEs at 100 m height and the one-
382 hour averaged US PFa LEs at 122 m height. However, the flight-level wavelet LEs do not match
383 the EC LEs at the flight level and US PFa tower height. The difference between airborne wavelet
384 LEs and airborne EC LEs may be due to the fact that wavelet LEs only consider the scales from
385 8 m to 8 km. The US PFa LEs are one-hour averaged EC LEs. The one-hour mean EC LEs
386 account for a footprint of 10-23 km, given the 2.9-6.4 m s⁻¹ averaged wind speeds (Table 1),
387 while the airborne wavelet-calculated LE represents about 23-30 km spatial distance in 5 minutes.
388 The tower measurements at a fixed point only represent a small area around the flux tower in the
389 footprint flux map (Figure 12 in Butterworth et al., 2021). As a result, the reason for the different
390 LEs obtained by the tower and airborne measurements could be that the aircraft measured
391 landscape-level LEs generated by local surface heterogeneities and mesoscale forcings in 30 x 30
392 km² extended domains.

393

394 3. Results

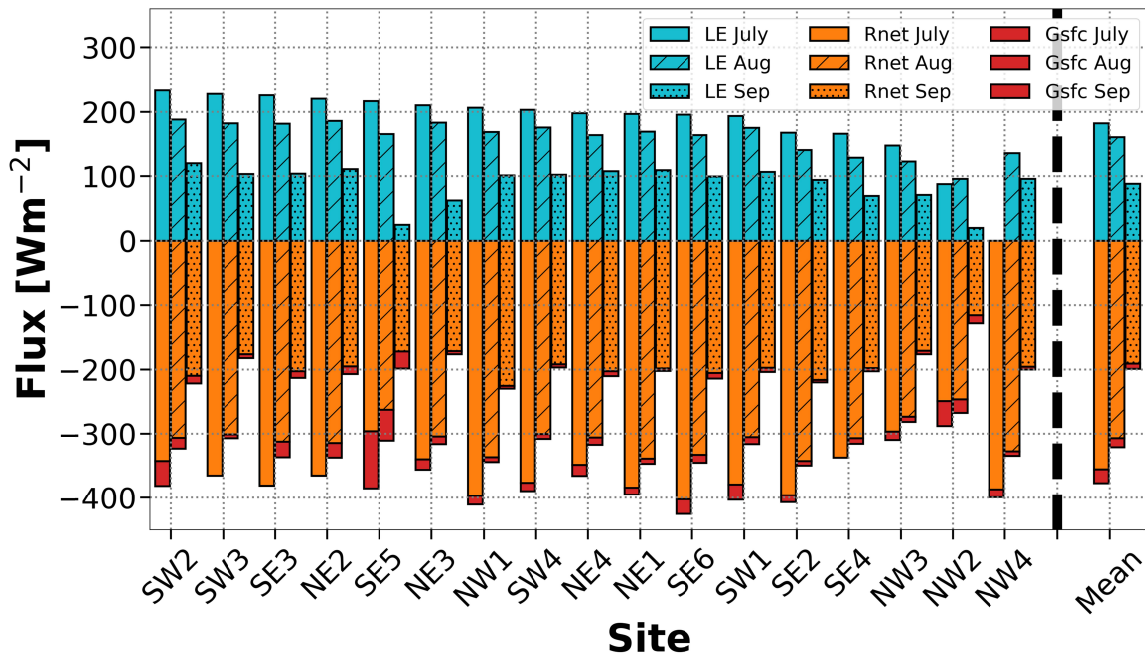
395

396 3.1 Surface Flux Variability Measured by Flux Towers

397

398 Seventeen ISFS flux towers provide continuous spatial flux records in the CHEESEHEAD19
399 domain throughout the campaign from July to September (Locations in Figure 1). Surface
400 heterogeneity influences the surface energy balance and resulting atmospheric responses in LE
401 variations. The full-monthly mean (30/31 days averaged value) R_{net} , ground heat flux (G_{sfc}),
402 and LE are calculated between 1300 and 0000 UTC to provide daytime fluxes in July, August,
403 and September, since the latest sunrise and earliest sunset time were 1252 and 0044 UTC on 28
404 September, respectively (all sunrise and sunset time shown in Table 1). The spatial incoming
405 available energy ($R_{net} + G_{sfc}$) varied from 425 Wm^{-2} to 290 Wm^{-2} in July, from 350 Wm^{-2} to 270
406 Wm^{-2} in August, and from 230 Wm^{-2} to 130 Wm^{-2} in September in a $10 \times 10 \text{ km}^2$ domain (Figure
407 4). The LE varied from 235 Wm^{-2} to 85 Wm^{-2} in July, from 190 Wm^{-2} to 95 Wm^{-2} in August, and
408 from 120 Wm^{-2} to 20 Wm^{-2} in September. These spatial variabilities of fluxes in the $10 \times 10 \text{ km}^2$
409 domain could come from the heterogeneous forested landscape, the topography of the surface,
410 and atmospheric responses from surface forcing. This deployment strategy reveals the variation
411 in surface and vegetation properties across the CHEESEHEAD19 domain. The tower-monthly
412 mean of incoming available energy and LE decreased from July to September (the last column in
413 Figure 4). The extended 3-month duration of the field experiment allows us to sample the
414 seasonal shift in the surface energy budget partitioning as the study domain shifts from a LE-
415 dominated late summer landscape to a greater sensible heat contribution early autumn landscape
416 (Butterworth et al., 2021).

417



418

419 **Figure 4.** The monthly-averaged daytime (1300 - 0000 UTC) LE, net radiation (Rnet), and
 420 ground heat flux (Gsfc) from the 17 EC towers and the 17-station mean values in July, August,
 421 and September. The sites are ordered with July LEs.

422

423 3.2. LE variability

424

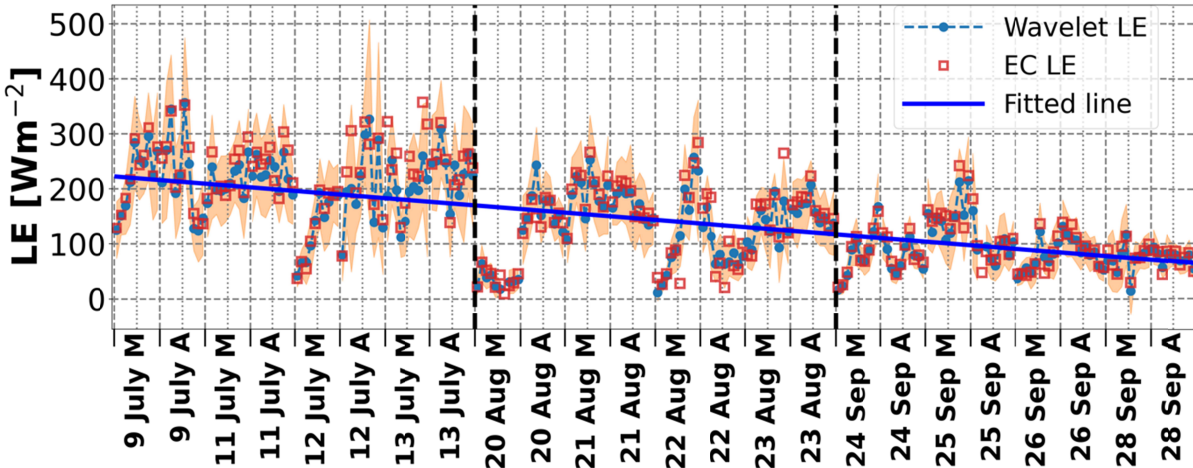
425 3.2.1 The temporal variability of leg-averaged LE

426

427 The leg-averaged LEs at the 100 m flight level reveal temporal variabilities. The leg-averaged
 428 LE is calculated by both wavelet (blue dots; by Equation S11) and EC (red squares; by Equation
 429 2) techniques for every flight leg, on both morning and afternoon RFs (Figure 5). The wavelet
 430 LEs are generally in good agreement with EC LEs through time. The orange-shaded areas
 431 represent the standard deviations of the wavelet LEs within the leg indicating spatial variabilities.
 432 The RF-average LE ranged from 250 Wm⁻² (12 July M and 22 August A), to 50 Wm⁻² (20
 433 August M and 28 September A) (Figure 5). These spatiotemporal variations reflect different
 434 surface types, wind conditions, and net radiation variations with time (Figure 1 and Table 1). The
 435 linear fit of leg-averaged LE indicates a decreasing trend from 210 to 80 Wm⁻² from July to

436 September (Figure 5). In summary, the leg-averaged LE decreased from July to September, but
 437 the diurnal and synoptic variations of LEs cannot be ignored.

438



439

440

441 *Figure 5. The leg-averaged LE was calculated by wavelet technique (blue dots) with their*
 442 *standard deviation (orange shaded area) and EC technique (red squares) on legs. The fitted line*
 443 *shown as the blue line represents the trend of the leg-averaged LE in RFs from July to*
 444 *September.*

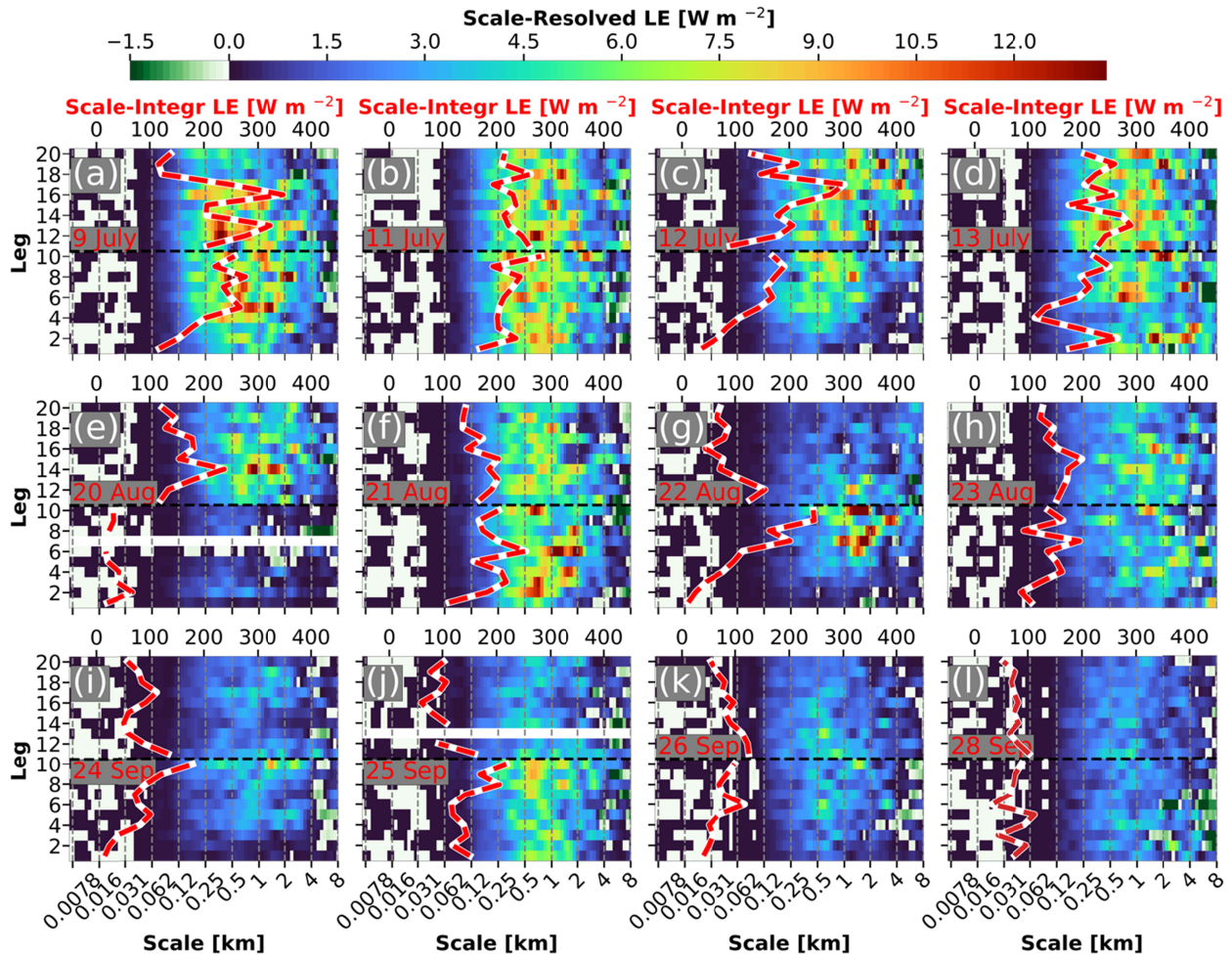
445

446 3.2.2 The Temporal Variability of Scale-resolved LE

447

448 The scale-resolved LE is calculated by Equation S11 for all flight legs to determine the scale
 449 contribution to the total LE over time and location. We examine all 12 days (Table 1), 4 from
 450 each IOP, each with a morning and an afternoon flight (Figure 6). The morning measurements
 451 include the first 10 flight legs, while the afternoon measurements consist of the last 10 flight legs
 452 in each day (Figure 6; separated by black dashed lines). The scale-resolved LE is averaged in
 453 each flight leg and is mostly between 62 m and 8 km as shown in Figure 6. The scale-resolved
 454 LE increases with time (leg number) as the total LE increases in the morning of 09 July, 12 July,
 455 22 August, and 24 September, while it decreases in the afternoon of 09 July, 20 August, 22
 456 August, and 26 September. However, these patterns are inconsistent for all dates, indicating the
 457 significant roles of PBL circulation and mesoscale advection in controlling local LEs other than
 458 radiation. The peak value of scale-resolved LE between 62 m to 8 km varies by as much as 10

459 Wm^{-2} on 12 July, 13 July, 20 August, and 22 August. The red-dashed lines represent the total LE.
 460 The daily temporal variation varies from 100 Wm^{-2} (28 September) to 280 Wm^{-2} (12 July).
 461 Although the total and scale-resolved LEs indicate strong temporal variation with legs, the
 462 primary scale is from 200 m to 4 km.
 463



464
 465 **Figure 6.** The leg-averaged LE distributions on the scale (x-axis) and leg number (y-axis) for
 466 dates of (a) 9, (b) 11, (c) 12, and (d) 13 July; (e) 20, (f) 21, (g) 22, and (h) 23 August; (i) 24; (j)
 467 25; (k) 26, and (l) 28 September. Legs 1-10 are for the morning, and Legs 11-20 are for the
 468 afternoon. The red-dashed lines represent the total LE (scale on upper x-axis).

469

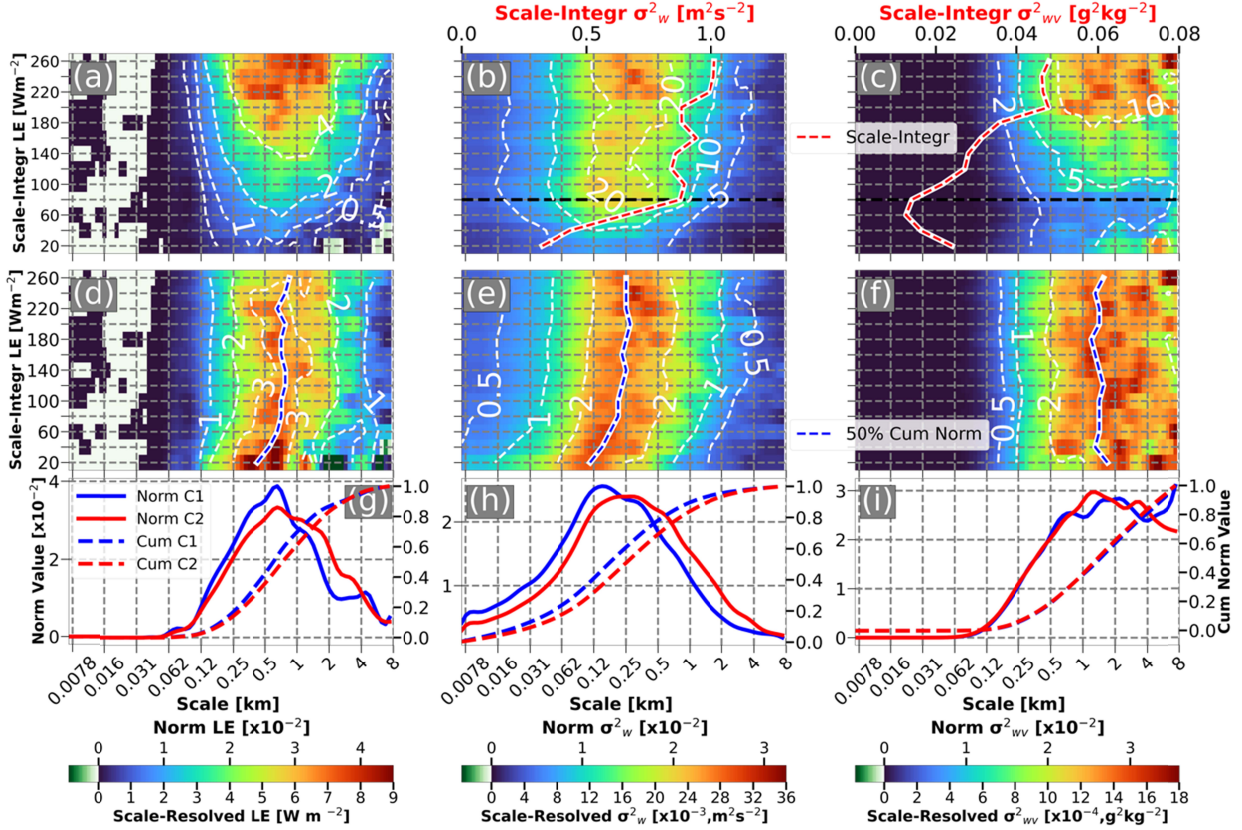
470 3.3 The Contributions of w' and r_v' on Scale-Resolved LE

471

472 3.3.1 Total LE Dependency

473
474
475
476
477
478
479
480
481
482
483
484
485
486
487
488
489
490

The scale-resolved LEs are composited at various total LEs ranging from 10-270 Wm^{-2} in 20 Wm^{-2} increments. The scale dependencies of LE, σ_w^2 , and σ_{wv}^2 from 7.8m to 8 km are depicted in Figures 7a-c. The distribution of scale-resolved LEs with values greater than 0.5 Wm^{-2} range from 200 m – 1.5 km to 100 m to 8 km, with the maximum scale-resolved LE increasing from 0.5 to 9 Wm^{-2} as the total LE linearly increases from 20 to 260 Wm^{-2} (white dashed contours in Figure 7a). Compared to the scale-resolved LE distributions, the scale-resolved σ_w^2 with values greater than $5 \times 10^{-3} \text{ m}^2 \text{ s}^{-2}$ is in smaller scale ranges from 50m-700m to 16 m - 4 km. The scale-resolved σ_{wv}^2 distribution with a value greater than $2 \times 10^{-4} \text{ g}^2 \text{ kg}^{-2}$ mainly focuses from 400 m - 8 km to 150 m - 8 km in scale as the total LE increases from 20 to 260 Wm^{-2} . As the total LE increases, the scale-resolved LE, σ_w^2 , and σ_{wv}^2 distributions extend to broader ranges. For LE increases between 20 and 100 Wm^{-2} , the total σ_w^2 (red dashed line in Figure 7b) quadruples (from 0.24 to 1.04 $\text{m}^2 \text{ s}^{-2}$), while the total σ_{wv}^2 (red dashed line in Figure 7c) remains steady (around 0.02 $\text{g}^2 \text{ kg}^{-2}$). The total σ_w^2 is nearly constant between 0.8 to 1.00 $\text{m}^2 \text{ s}^{-2}$ as the total LE increases from 100 to 260 Wm^{-2} . However, the total σ_{wv}^2 linearly increases from 0.018 to 0.048 $\text{g}^2 \text{ kg}^{-2}$ from 100 to 220 Wm^{-2} . The characteristics of σ_w^2 and σ_{wv}^2 variations show the dominance of σ_w^2 for low LE periods and the dominance of σ_{wv}^2 for high LE periods.



491
 492 **Figure 7.** The scale-dependent (a) LE, (b) σ_w^2 , and (c) σ_{wv}^2 , and normalized scale-dependent (d)
 493 LE, (e) σ_w^2 , and (f) σ_{wv}^2 distributions as a function of leg-integrated total LE from 20 to 260
 494 Wm^{-2} ; The distributions of normalized scale-dependent and cumulative (g) LE, (h) σ_w^2 , and (i)
 495 σ_{wv}^2 for low-LE (from 20 to 80 Wm^{-2}) legs, referred to as C1, and for high-LE (from 100 to 260
 496 Wm^{-2}) legs, referred to as C2. The white dashed contours in (a)-(f) represent the normalized
 497 values (see color bar below). The red-dashed lines in (a)-(c) represent the leg-averaged scale-
 498 integrated values; the blue dashed lines in (d)-(f) represent the scale of the median LE scale (50%
 499 cumulative values).

500
 501 It is difficult to investigate the relative scale contributions of σ_w^2 , and σ_{wv}^2 to LE due to their
 502 value and scale-range variations as the total LE increases in Figure 7a-c. To address this issue,
 503 the scale-resolved LE, σ_w^2 , and σ_{wv}^2 are normalized based on Equations S10 and S12. The 50 %
 504 value in the cumulative normalized scale-resolved LE, σ_w^2 , and σ_{wv}^2 are marked as blue dashed
 505 lines (Figure 7d-f). The distribution of normalized scale-resolved LE with values greater than 1%
 506 shifts from 120 m – 1.5 km to 250 m – 2 km as the total LE increases from 20 to 260 Wm^{-2}

507 (Figure 7d). In the meantime, the normalized scale-resolved σ_w^2 with values greater than 1%
508 range shifting from 16 m – 800m to 50 m to 2 km, and the normalized scale-resolved σ_{wv}^2 with
509 values greater than 0.5% ranges from 150 m to 8 km as the total LE increases. The 50%
510 cumulative normalized scale-resolved LE is located in scale from 420 m to 700 m as total LE
511 increases from 20 to 80 Wm^{-2} and then maintains its scales at ~ 700 m from 100 – 260 Wm^{-2} . The
512 50% cumulative normalized scale-resolved σ_w^2 also has an increasing trend in the scale from 120
513 m to 250 m as total LE from 20 to 120 Wm^{-2} and then maintains its location around 250 m as
514 total LE increases to 260 Wm^{-2} . The scale of 50% cumulative normalized scale-resolved σ_{wv}^2 is
515 located around 1.2 -1.7 km without an increasing trend.

516

517 Based on normalized and cumulative values, the scale-resolved LEs are divided into two
518 categories. The first category (C1) contains low total LE 100 m AGL flight legs (between 20 and
519 80 Wm^{-2}), while the second category (C2) contains high total LE values (between 100 and 260
520 Wm^{-2}), as shown in Figures 7g-i. The normalized scale-resolved LE in C1 is larger than that in
521 C2 in scales ranging from 250 m to 800 m, while normalized scale-resolved LE in C2 is larger
522 than that in C1 in scales ranging from 800 m to 4 km. The same pattern is observed in the
523 distribution of normalized scale-resolved σ_w^2 , but with the separation scale at 250 m (Figures 7g
524 and 7h). The distribution of normalized scale-resolved LE and σ_w^2 are different for the two
525 categories. However, the normalized scale-resolved σ_{wv}^2 has the same values from 8 m to 800 m
526 in C1 and C2. The cumulative normalized values show the percentage of resolved scales in LE,
527 σ_w^2 , and σ_{wv}^2 .

528

529 Operational numerical weather prediction (NWP) systems can use scale-resolved normalized and
530 cumulative values to guide sub-grid scale parameterization. The highest resolution operational
531 non-hydrostatic NWP systems approach horizontal grid spacings of 1.0 km, e.g. the Application
532 of Research to Operations at Mesoscale (AROME) runs at 1.2 km, and the Consortium for
533 Small-scale Modeling (COSMO) runs at 1.1 km in parts of Europe (e.g., Benjamin et al. (2019);
534 Dowell et al. (2022)). In general, the effective model resolution is coarser than the grid spacings.
535 If we assume that 6 grid points are needed to adequately resolve a wavelike phenomenon
536 (Benjamin et al. 2019), the smallest resolvable feature in a 1 km grid model is 6 km (e.g.,
537 Chapter 11 in Lackmann 2011). The spectral distribution in Figure 7 indicates that the

538 unresolvable normalized percentages are 87-89% in LE, 95-97% in σ_w^2 , and 66-68% in σ_{wv}^2 for
539 the highest resolvable resolution of 6 km in the highest-resolution NWP systems currently in
540 operation. The high unresolvable normalized percentages indicate LE and σ_w^2 are dominated
541 more by the forcings on smaller scales, compared to that in σ_{wv}^2 . Thus, the unresolvable scale-
542 dependent values driven by scales smaller than NWP resolution must be carefully parameterized
543 in the NWP systems.

544

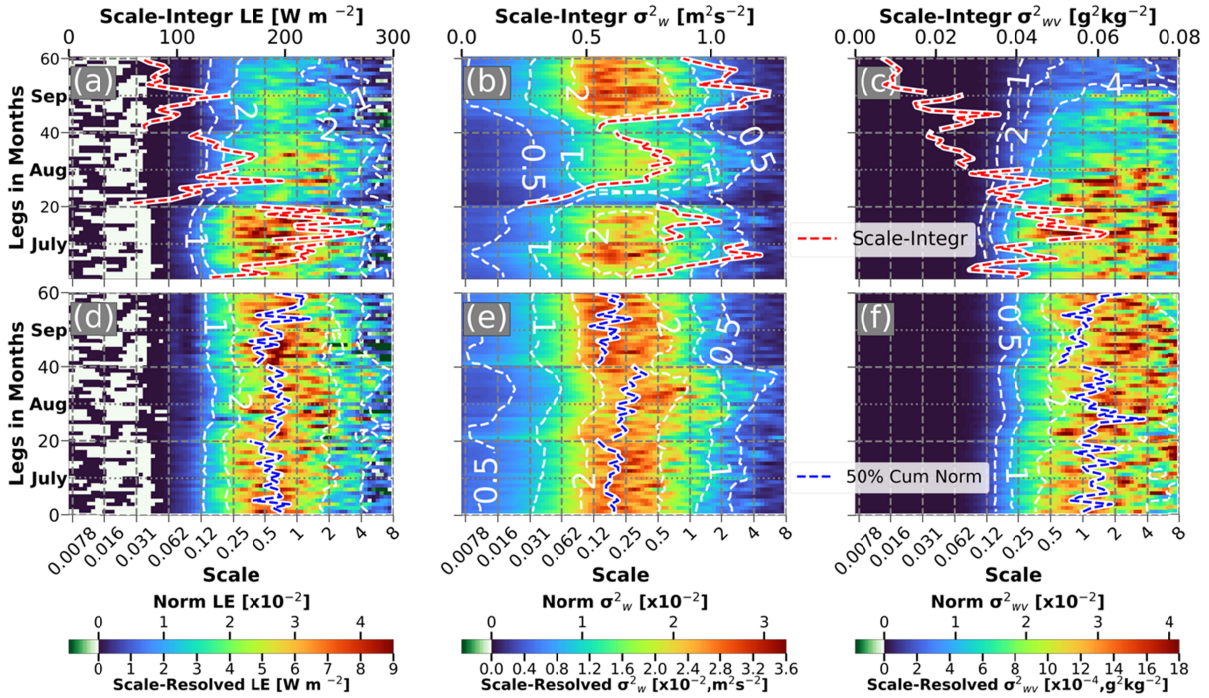
545

546 **3.3.2 Temporal dependency**

547

548 To investigate the temporal variability of scale-resolved LE, σ_w^2 , and σ_{wv}^2 , the LE is composited
549 on 20 flight legs from morning to afternoon in flight IOPs of July, August, and September
550 (Figures 8a-c). Even though the first flight took off at different times and the sunrise and sunset
551 times varied in RFs of IOPs from July to September (Table 1), the same legs from all four RFs in
552 the morning and in the afternoon in each IOP are averaged. The distribution of scale-resolved LE
553 with values greater than 2 Wm^{-2} is shrunk from 120 m - 4 km in July to 250 m - 2 km in
554 September, showing flight-leg dependent temporal variability in each month (Figure 8a).
555 Similarly, the distribution of scale-resolved σ_{wv}^2 with values greater than $10^{-4} \text{ g}^2\text{kg}^{-2}$ shrunk
556 ranging from 120 m - 8 km in July to 250m - 4km in September (Figure 8c). However, the
557 distribution of scale-resolved σ_w^2 differs from that in scale-resolved LE and σ_{wv}^2 , with values
558 greater than $0.5 \times 10^{-3} \text{ m}^2\text{s}^{-2}$ observed in 32 m - 4 km in August, but shifts to 10 m - 3 km in July
559 and September.

560



561
 562 **Figure 8.** As in Figure 7 (a)-(f), but as a function of *leg numbers* (*y-axis*) averaged *monthly IOPs*
 563 *in July, August, and September.*

564
 565 To investigate the relative scale distributions of LE, σ_w^2 , and σ_{wv}^2 , the normalized scale-resolved
 566 LE, σ_w^2 , and σ_{wv}^2 are calculated based on legs in IOPs. The range of normalized scale-resolved
 567 LEs is from 120 m to 4 km for values greater than 1% of the cumulative normalized LE, and for
 568 values greater than 2% range from 200 m to 2 km (Figure 8d). In August, the scale range of
 569 normalized scale-resolved LE with values greater than 1% shifted from 120 m – 4 km in July and
 570 September to 160 m – 6 km. The temporal variation is shown as the scale of 50% of cumulative
 571 normalized scale-resolved LE (blue dashed lines in Figure 8d-f). The scale of 50% of cumulative
 572 normalized scale-resolved LE ranges from 350 m to 700 m in July, 500 m – 840 m in August,
 573 and 350 m to 1.2 km in September. In the meantime, the normalized scale-resolved σ_w^2
 574 distribution is mainly located between 32 m and 2 km (Figure 8e). The distribution of normalized
 575 scale-resolved σ_w^2 with values greater than 1% among IOPs has a similar scale distribution to the
 576 normalized scale-resolved LE with a larger scale range in August than that in July and
 577 September. The scale of 50% of cumulative normalized scale-resolved σ_w^2 varies from 130 m to
 578 210 m in July, 200 m – 350 m in August, and 100 m to 270 m in September. The normalized
 579 scale-resolved σ_{wv}^2 with a value greater than 1% ranges between 200 m and 8 km (Figure 8f).

580 The scale of 50% of cumulative normalized scale-resolved σ_{wv}^2 varies from 1 km to 2 km in July,
581 700 m – 3.6 km in August, and 600 m to 2.6 km in September. Even though strong temporal
582 variations exist in flight legs and in IOPs, the mean scale of 50% of the cumulative normalized
583 scale-resolved value is 640 m of LE, 200 m of σ_w^2 , and 1.25 m of σ_{wv}^2 , respectively. The
584 primary contribution to scale-resolved LE should be in the overlap scales between σ_w^2 (32 m – 2
585 km) and σ_{wv}^2 (200 m – 8 km) ranging between 200 m and 2 km, which coincides with the
586 primary scale-resolved LE distribution with values greater than 2% ranging from 200 m to 2 km.
587 Despite the different scale distribution between σ_w^2 and σ_{wv}^2 , the primary scale contribution
588 between 200 m and 2 km from σ_w^2 and σ_{wv}^2 to LE indicates large eddies in the PBL primary
589 sources of vertical moisture transport.

590

591

592 **3.4 The Contributions of Turbulent, Large, and Mesoscale Eddies on LE**

593

594 **3.4.1 Total LE Dependency**

595

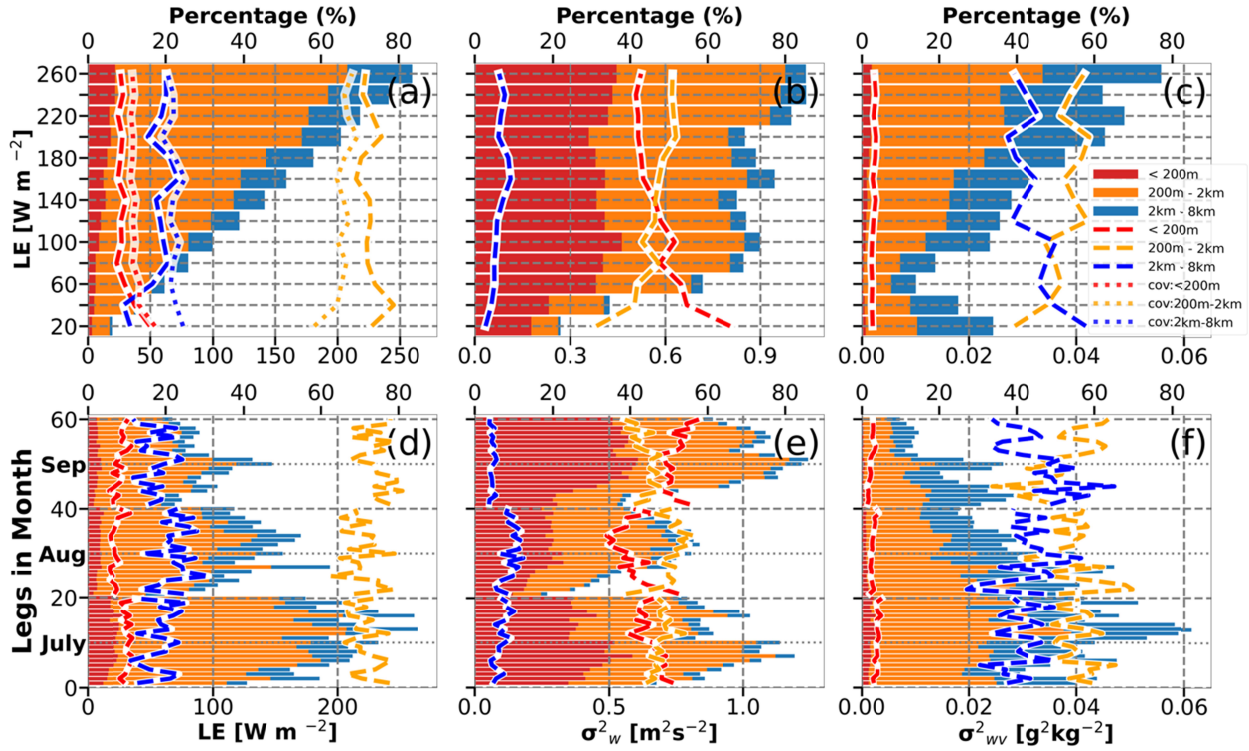
596 To better understand the scale-dependent impacts of w' and r_v' to LE, the scales from 8m to 8 km
597 are classified into three ranges. Previous studies (e.g., Mauder et al., 2007; Paleri et al., 2022)
598 used a 2 km threshold to divide the scales into the turbulent scale in PBL and mesoscale to
599 investigate mesoscale contributions to the total LE. Our analysis of scale-resolved σ_w^2 shows that
600 the primary scale-resolved σ_w^2 occurs within a wavelength of 2 km (Figure 7e and Figure 8e),
601 which aligns with the PBL depth. Orlandi (1975) used a threshold scale of 200 m to
602 differentiate between turbulence (micro β scale < 200 m) and organized eddies (micro α scale $>$
603 200 m). Our analysis of scale-resolved σ_{wv}^2 shows that the 200 m marks the beginning of the
604 σ_{wv}^2 scale contributing to LE. Thus, the scales are divided into three ranges: 8 m - 200m
605 (turbulent scale in PBL), 200 m – 2 km (large-eddy scale in PBL), and 2 km – 8 km (mesoscale)
606 to explore their contributions to σ_w^2 , σ_{wv}^2 , and LE under different total LE values and IOP legs.
607 Note that both the turbulent and large-eddy scales fall in the inertial subrange for isotropic
608 turbulence in the surface layer (Stull 1988).

609

610 The scale-resolved LE in the three scale ranges increases as the total LE increases from 20 to 260
611 Wm^{-2} , but the percentage contributions to total LE among the three scale ranges only slightly
612 change (Figure 9a). The large-eddy scale contributes to the highest percentage of total LE,
613 ranging from 69 to 75 % (the orange dashed line in Figure 9a). The mesoscale contributes to the
614 second largest percentage of total LE, ranging from 9% to 23 % (the blue dashed line). The
615 turbulent-scale eddy only contributes 8 -15 % of the total LE (the red dashed line). The majority
616 of the σ_w^2 is found in turbulent and large eddy scales, accounting for over 90% of the total σ_w^2 .
617 As the total LE increases from 20 to 260 W m^{-2} , the turbulent σ_w^2 decreases from 65% to 42%,
618 while the σ_w^2 in the large-eddy scale increases from 31% to 51%. The mesoscale σ_w only
619 contributes 3% -9% of the total σ_w^2 . On the other hand, the σ_{wv}^2 is mainly found in the large-
620 eddy scale and mesoscale, accounting for over 96% of total σ_{wv}^2 , while the turbulent scale σ_{wv}^2 is
621 only 3-4% of total σ_{wv}^2 , which could be biased by the temporal response of the water vapor
622 sensor.

623
624 To examine the scale contribution from the covariance of w' and r_v' to the LE, $\text{cov}_{(w,wv)}$ in the
625 three scale ranges is calculated based on Equation S13 (dotted lines in Figure 9a). The largest
626 difference between $\text{cov}_{(w,wv)}$ and LE is observed in the large-eddy scale, accounting for 7.2%
627 mean percentage of total LE. The mean difference in turbulent scale and mesoscale is 2.9% and
628 4.3% of total LE, respectively. The most significant difference is observed in the total LE
629 between 20 and 60 Wm^{-2} , particularly the difference is 15% in the mesoscale as the total LE
630 ranges from 20 to 40 Wm^{-2} . Overall, the analysis of $\text{cov}_{(w,wv)}$ revealed similar results to the
631 directly calculated LE, with the majority of LE (58-68%) found in the large-eddy scale, followed
632 by the mesoscale (21-25%), and the smallest percentage (8-15%) of the total LE found in the
633 turbulent scale.

634



635
 636 **Figure 9.** The partitions of turbulent scale (red), large eddy scale (orange), and mesoscale (blue)
 637 contributions based on leg-integrated LE in LE (a and d), σ_w^2 (b and e) and σ_{wv}^2 (c and f) sorted
 638 with LE from 20 -260 Wm^{-2} (a-c) and leg time (d-f). The red-, orange-, and blue-dashed lines
 639 represent the leg-averaged scale-integrated contributions (expressed as percentages) from
 640 turbulent scale, large-eddy scale, and mesoscale respectively. The dotted lines in (a) are the
 641 corresponding $cov_{(w,wv)}$ averages in the three scale ranges.

642

643 3.4.2 Temporal dependency

644

645 The contributions in different scale ranges to monthly IOP-mean total LEs are similar to the
 646 previous analysis, but temporal variations exist in legs and in IOPs (Table 3 and Figures 9d-f).
 647 The turbulent scale contributions in LE vary from 10.2 % to 7.0 % from July to September. The
 648 large-eddy scale contributions in LE vary from 70.4% to 74.7 % from August to September. The
 649 mesoscale contributions vary from 22.6% to 17.0% from August to September. In monthly IOP-
 650 mean σ_w^2 variations, the turbulent scale contributions vary from 40.5% to 51.6%. The large-eddy
 651 scale contributions vary from 50.3% to 43.9%, and the mesoscale contributions vary from 9.2%
 652 to 4.4 %. In the monthly IOP-mean σ_{wv}^2 variation, the turbulent scale contributions vary from 4.0%

653 to 2.3 %. The large-eddy scale contributions vary from 55.2 % to 51.8 %, and the mesoscale
654 contributions vary from 40.8% to 45.9%. The monthly IOP-mean variations range from 3.2 % to
655 5.6% in LE, from 6.4 % to 11.1% in σ^2_w , and 1.7% to 5.1% in σ^2_{wv} in the three scale ranges.

656

657 **Table 2:** *The monthly leg-averaged mean and the standard deviation in LE, σ^2_w , and σ^2_{wv} in*
658 *three spatial ranges (turbulent scale, large-eddy scale, and mesoscale), expressed as a*
659 *percentage of the total.*

660

661

Variable		July		Aug		Sep	
		Mean	Std	Mean	Std	Mean	Std
LE	Turb (%)	10.2	1.3	7.0	1.2	8.3	1.5
	Large-eddy (%)	71.3	3.8	70.4	4.4	74.7	3.9
	Meso (%)	18.4	4.3	22.6	4.4	17.0	4.0
σ^2_w	Turb (%)	45.5	3.0	40.5	4.7	51.6	2.9
	Large-eddy (%)	47.7	2.2	50.3	3.7	43.9	2.8
	Meso (%)	6.8	1.6	9.2	2.1	4.4	0.6
σ^2_{wv}	Turb (%)	4.0	0.6	2.8	0.6	2.3	0.7
	Large-eddy (%)	55.2	4.8	54.6	6.9	51.8	7.8
	Meso (%)	40.8	5.0	42.6	7.1	45.9	8.3

662

663 The temporal variations in legs are represented by standard deviations. The major temporal
664 variations in legs are in the largest and second-largest scale ranges of LE (the large-eddy scale
665 and mesoscale), σ^2_w (the turbulent and large-eddy scales), and σ^2_{wv} (the large-eddy scale and
666 mesoscale) shown in Figures 9d-f. The temporal LE variations in the large-eddy scale and
667 mesoscale LE have standard deviations of 3.8% – 4.3%. The temporal σ^2_w variations in turbulent
668 and large-eddy scales range from 2.2 % to 4.7%. The temporal σ^2_{wv} variations in the large-eddy
669 scale and mesoscale range between 4.8% and 7.8%. The smallest temporal variations in legs are
670 1.2%-1.5% in turbulent LE, 0.6%-2.1% in mesoscale σ^2_w , and 0.6%-0.7% in turbulent σ^2_{wv} .

671

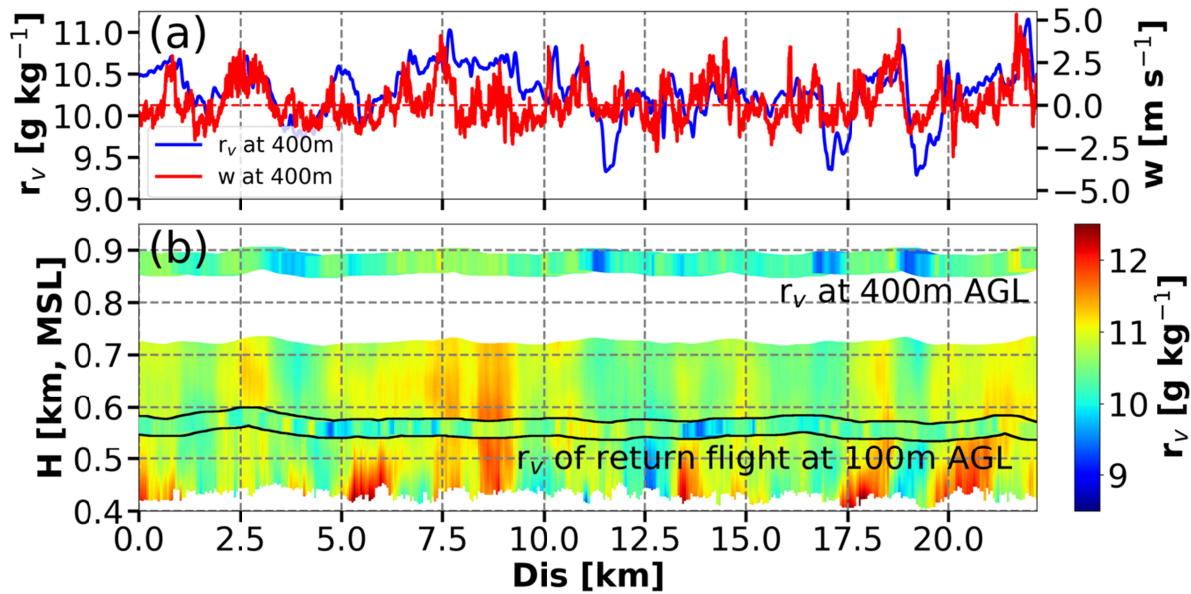
672

673 3.5 Forcing scales of w' and rv' : Implications and Additional Evidence

674

675 Results above indicated that the scale forcings are different in σ_w^2 , and σ_{wv}^2 to LE. The primary
676 scale forcings are the large-eddy scale and mesoscale in LE, the turbulent scale and large-eddy
677 scale in σ_w^2 , and the large-eddy scale and mesoscale in σ_{wv}^2 . Couvreux et al. (2005) and
678 Couvreux et al. (2006) investigated r_v variability in the convective boundary layer (CBL) with
679 airborne measurements and large eddy simulations (LES) and also found that the characteristic
680 length scale of r_v is larger than w . Both observations and LES indicate the intrusions of dry free-
681 troposphere air into the growing CBL. These intrusions generally lack negative buoyancy but
682 they may interact with large-eddy circulations that transport the drier free-troposphere into the
683 lower CBL, and occasionally even close to the surface. Moreover, Couvreux et al. (2005) and
684 Couvreux et al. (2006) found that large amounts of dry air that are quickly incorporated into the
685 CBL prevent full homogenization by turbulent mixing. Near the heated land surface, these dry
686 air intrusions may become negatively buoyant. In our study, the flight tracks at 400 m AGL with
687 CRL measurements provide 2D vertical profiles of r_v to investigate the vertical r_v distribution and
688 transport process (Figure 10). For instance, the 400 m AGL flight in situ data measured
689 downward transport (negative flight-level w) of relatively drier air ($\sim 9.2 \text{ g kg}^{-1}$) at the distance of
690 11.5 km, 17 km, and 18.5 km (Figure 10a). The CRL sampled these three drier air parcels and
691 shows that they penetrated toward the 100 m AGL (Figure 10b). The horizontal scales of dry and
692 moist air parcels (PBL large eddies) sampled by CRL are a few kilometers, which is consistent
693 with the return flight-level σ_{wv}^2 scaling from 200 m – 8 km at 100 m AGL in Figure 2i,
694 indicating large-eddy and mesoscale forcings in r_v . Since the time difference between the two
695 flight legs is 5- 10 minutes, and the chosen RFs that are closest perpendicular to the prevailing
696 wind, the r_v at 100 m AGL between CRL and flight level data do not correspond very well.
697 However, r_v shows a shift of dry air ($\sim 9 \text{ g kg}^{-1}$) from 12.5 km for the CRL measurement to 13.5
698 km for the airborne in situ measurement at around 100 AGL. Although lacking 2D w' profiles
699 from the airborne measurements, variability in w' at smaller scales than r_v' is observed at 400 m
700 AGL (Figure 10a). Moreover, w' at the 100 m return flight shows small-scale variability between
701 16 m and 1.5 km (Figure 2h) indicating the dominant turbulent and large-eddy scale forcings.

702



703
 704 **Figure 10.** (a) Flight-level r_v (blue line) and w (red line) for RF03 leg 2 at 400 m. (b) Flight-
 705 level in situ r_v and CRL 2D profile of r_v . Since the surface height varies along the flight track, the
 706 2D r_v profile uses mean sea level (MSL) as the height reference. The colored return flight at 100
 707 m AGL is the r_v along the flight leg in Figure 2, where the flight track is the same as this flight,
 708 but at a different height.
 709

710 4. Discussion

711
712 The leg-averaged and scale-resolved LE show seasonal variations from July to September. The
713 leg-averaged LE was up to 250 Wm^{-2} in a single 3-hour RF, and the leg-averaged LE decreased
714 from July to September. The scale-resolved LE in RFs mainly distributes between 62 m and 8
715 km with scale-resolved temporal variability. However, the general diurnal patterns of leg-
716 averaged LE didn't occur for all IOP days highlighting the significant roles of PBL circulation
717 and mesoscale advection in controlling local LEs other than radiation. These temporal variations
718 are related to the combination of differences in surface types, wind conditions, and net radiation
719 as the aircraft samples in space and time and require rectification and footprint-identification
720 approaches for any mapping of LE using airborne data (Metzger et al., 2013; Sun et al., 2023).

721
722 The primary transport process in the PBL is turbulent-driven fluxes, which can be directly
723 measured by the EC technique. The mesoscale forcing is not adequately resolved by traditional
724 EC measurement due to short averaging times, surface heterogeneity, PBL circulation, and lack
725 of closure in the energy budget (Mauder et al., 2006; Sun et al., 2006; Mahrt, 2010; Foken et al.,
726 2011; Charuchittipan et al., 2014; Butterworth et al., 2021). Hence the expected value from a
727 single-tower measurement tends to systematically underestimate the surface heat flux. Compared
728 to shortcomings in conventional EC measurements, large eddy simulation (LES) studies can
729 advance the understanding of scale-dependent physical processes in fluxes that EC tower
730 measurements cannot resolve. Margairaz et al. (2020) investigated organized PBL circulations
731 over the heterogeneous surface over a broad range of atmospheric stability conditions in LES.
732 Couvreux et al. (2005) used airborne measurements and LES to investigate r_v variability in PBL
733 at the large-eddy scale and sub-mesoscale (a few kilometers) in the convective boundary layer
734 (CBL). The vertical transport associated with the large eddy to mesoscale circulations could be
735 missed by single tower-based measurements, and it can be overestimated if the tower happens to
736 be located near mesoscale boundaries (Mahrt, 2010; Charuchittipan et al., 2014; Helbig et al.,
737 2021).

738
739 The wavelet technique applied to high-frequency airborne data allows us to analyze atmospheric
740 flux contributions from the turbulent scale to the mesoscale above heterogeneous terrain during

741 the CHEESEHEAD19 field campaign. The covariance of w' and r_v' impacts the LE at different
742 scales with temporal variability. The scale distribution of LE, σ_w^2 , and σ_{wv}^2 are different, with the
743 dominant scales ranging from 120 m to 4 km for LE, from 32 m to 2 km for σ_w^2 , and from 200 m
744 to 8 km for σ_{wv}^2 . The primary contribution to scale-resolved LE should be in the overlap scales
745 between σ_w^2 and σ_{wv}^2 ranging between 200 m and 2 km, which coincides with the primary scale-
746 resolved LE distribution. The temporal variation is shown as the scale of 50% of cumulative
747 normalized scale-resolved values. In these terms, the 50% scale (or median scale) ranges from
748 350 m to 1.2 km (3-IOP mean: 640 m) for LE, from 130 m to 200 m – 350 m (mean: 200 m) for
749 σ_w^2 , and from 600 m to 3.6 km (mean: 1250 m) for σ_{wv}^2 . The different scale distributions of LE,
750 σ_w^2 , and σ_{wv}^2 suggest that large eddies in the 200 m - 2 km width range are the primary sources
751 of vertical moisture transport across the PBL, despite different scale contributions of σ_w^2 and
752 σ_{wv}^2 .

753
754 We defined the turbulent, large-eddy, and mesoscale as 8 m - 200 m, 200 m – 2 km, and 2 - 8 km
755 respectively. 85-92 % of total LE falls in large-eddy scale and mesoscale, 90% of the total σ_w^2
756 falls in turbulent scale and large-eddy scale, and 96% of the total σ_{wv}^2 falls in large-eddy scale
757 and mesoscale. Most variance in LE, σ_w^2 , and σ_{wv}^2 is found in the large-eddy scale, with 69-75 %
758 of total LE, 31-51% of the total σ_w^2 , and 39-59 % of the total σ_{wv}^2 . The temporal monthly IOP-
759 mean variations range from 1.7% to 11.1% of total values. The temporal variations in legs are
760 represented by standard deviations ranging from 0.6% -7.8% of total values. Although diurnal
761 and seasonal LE variation exists, this finding implies the dominance of the large eddy scale for
762 LE, driven by a combination of w' and r_v' variations.

763
764 This large-eddy scale in PBL is not captured even by the finest-resolution operational regional
765 non-hydrostatic NWP systems currently in operation, with horizontal grid spacings near 1 km
766 (Dowell et al., 2022). The unresolved cumulative normalized percentages within scales less than
767 6 km (the minimum size of a feature resolved by a 1 km grid) are 99% in LE, 99% in σ_w^2 , and
768 94-96% in σ_{wv}^2 . These high percentages of unresolvable scale-dependent values driven by scales
769 smaller than NWP resolution explain the continued need for PBL parameterizations in NWP
770 models.

771
772 This observational study describes the spatiotemporal LE variation and the impacts of w and r_v
773 during the CHEESEHEAD19 field campaign. The large-eddy transport process contributes most
774 of the total LE across the daytime PBL in the summer of northern Wisconsin. This analysis
775 complements published LE variations on scales, which primarily present scale-dependent LE
776 analysis and lack detailed scale-dependent vertical velocity and water vapor contributing
777 information to LE.

778
779 The dominant scales of LE, w , and r_v are height-dependent, as evident from airborne
780 measurements and LES simulations (Couvreur et al., 2005). The w and r_v in PBL are determined
781 by not only surface evapotranspiration, but entrainment from the free atmosphere, PBL
782 circulation and depth, and mesoscale advection (Linné et al., 2006). Future studies should further
783 explore the height-dependent scale-resolved LE and the impacts of w and r_v on LE by applying
784 the wavelet technique to airborne in situ data collected at multiple flight levels, or, better, by
785 combining full profiles of airborne Raman lidar r_v data with Doppler lidar w measurements.

786

787 **5. Conclusions**

788

789 This study uses airborne measurements collected during the CHEESEHEAD19 field experiment
790 to quantify the multi-scale diurnal and seasonal variation of latent heat flux (LE) and of its
791 components (w and r_v) over a heterogeneous surface in northern Wisconsin from July to
792 September 2019. Wavelet analysis of high-frequency measurements along the 25-30 km airborne
793 tracks is used to evaluate characteristic scales of LE and its components, w and r_v , in the range
794 of 8 m to 8 km. All data were collected during the daytime, under fair-weather conditions, at 100
795 m AGL, or roughly 3-4 times the tree canopy height. The two main conclusions are as follows:

796

- 797 - The dominant scale is rather short for w (32 m – 2 km), longer for r_v (200 m to 8 km), and
798 intermediate for LE (120 m to 4 km), which depends on the covariance of w and r_v .
- 799 - Most variance in LE, σ_w^2 , and σ_{wv}^2 is found in the large-eddy scale, which we define as
800 between 0.2 – 2.0 km, with σ_w^2 containing substantial variability also in the turbulent
801 scale (8 m – 200 m in this study) and σ_{wv}^2 in the mesoscale (2-8 km in this study).

802

803 Clearly, the PBL will need to be parameterized in NWP models in the foreseeable future. Further
804 studies should compare the different atmospheric fluxes between the airborne measurements and
805 model simulation to improve the parameterization of PBL fluxes (Hu et al., 2023).

806 *Acknowledgments.* This study was funded and supported by the National Science Foundation
807 (NSF) Grants AGS-1917693 and AGS-1917701, by the Department of Energy (DOE)
808 Atmospheric System Research (ASR) Grant SC0020171, and by the National Aeronautics and
809 Space Administration (NASA) 80NSSC20K0663, with additional support for scientific airborne
810 data collection activities from the University of Wyoming King Air team. The
811 CHEESEHEAD19 field campaign was supported by NSF Grant AGS-1822420. US-PFa
812 observations were supported by a subaward to Desai from the DOE Ameriflux Network
813 Management Project. The CHEESEHEAD19 data are provided by NSF-funded NCAR/EOL via
814 the respective projects' Field Catalogs. The present study benefitted from the hard work of the
815 many additional CHEESEHEAD19 participants to collect the data that helped enable this study.

816

817 *Data availability statement.* The UWKA in situ data and surface-based flux tower data are
818 available on the EOL CHEESEHEAD website
819 (https://www.eol.ucar.edu/field_projects/cheesehead). The land cover classification of NLCD
820 2019 can be found on the Multi-Resolution Land Characteristics Consortium (MRLC) website
821 (<https://www.mrlc.gov/data/nlcd-2019-land-cover-conus>).

822

823 **References**

824

- 825 Attié, J.-L., & Durand, P. (2003), Conditional Wavelet Technique Applied to Aircraft Data
826 Measured in the Thermal Internal Boundary Layer During Sea-Breeze Events. *Boundary-*
827 *Layer Meteorology*, 106(3), 359-382. <https://doi.org/10.1023/a:1021262406408>.
- 828 Aubinet, M., Vesala, T., & Papale, D. (2012), Eddy covariance: A practical guide to
829 measurement and data analysis. <https://doi.org/10.1007/978-94-007-2351-1>.
- 830 Avissar, R., & Schmidt, T. (1998), An Evaluation of the Scale at which Ground-Surface Heat
831 Flux Patchiness Affects the Convective Boundary Layer Using Large-Eddy Simulations.
832 *Journal of the Atmospheric Sciences*, 55(16), 2666-2689. [https://doi.org/10.1175/1520-](https://doi.org/10.1175/1520-0469(1998)055<2666:Aeotsa>2.0.Co;2)
833 [0469\(1998\)055<2666:Aeotsa>2.0.Co;2](https://doi.org/10.1175/1520-0469(1998)055<2666:Aeotsa>2.0.Co;2).
- 834 Bange, J., Beyrich, F., & Engelbart, D. A. M. (2002), Airborne measurements of turbulent fluxes
835 during LITFASS-98: Comparison with ground measurements and remote sensing in a
836 case study. *Theoretical and Applied Climatology*, 73(1), 35-51.
837 <https://doi.org/10.1007/s00704-002-0692-6>.
- 838 Benjamin, S. G., Brown, J. M., Brunet, G., Lynch, P., Saito, K., & Schlatter, T. W. (2019), 100
839 Years of Progress in Forecasting and NWP Applications. *Meteorological Monographs*,
840 59, 13.11-13.67. <https://doi.org/10.1175/amsmonographs-d-18-0020.1>.
- 841 Berger, B. W., Davis, K. J., Yi, C., Bakwin, P. S., & Zhao, C. L. (2001), Long-Term Carbon
842 Dioxide Fluxes from a Very Tall Tower in a Northern Forest: Flux Measurement
843 Methodology. *Journal of Atmospheric and Oceanic Technology*, 18(4), 529-542.
844 [https://doi.org/10.1175/1520-0426\(2001\)018<0529:Ltcdff>2.0.Co;2](https://doi.org/10.1175/1520-0426(2001)018<0529:Ltcdff>2.0.Co;2).
- 845 Beyrich, F., Herzog, H. J., & Neisser, J. (2002), The LITFASS project of DWD and the
846 LITFASS-98 experiment: The project strategy and the experimental setup. *Theoretical*
847 *and Applied Climatology*, 73(1-2), 3-18. <https://doi.org/10.1007/s00704-002-0690-8>.
- 848 Beyrich, F., & Mengelkamp, H.-T. (2006), Evaporation over a Heterogeneous Land Surface:
849 EVA_GRIPS and the LITFASS-2003 Experiment—An Overview. *Boundary-Layer*
850 *Meteorology*, 121(1), 5-32. <https://doi.org/10.1007/s10546-006-9079-z>.
- 851 Bou-Zeid, E., Anderson, W., Katul, G. G., & Mahrt, L. (2020), The Persistent Challenge of
852 Surface Heterogeneity in Boundary-Layer Meteorology: A Review. *Boundary-Layer*
853 *Meteorology*, 177(2-3), 227-245. <https://doi.org/10.1007/s10546-020-00551-8>.

854 Butterbach-Bahl, K., Kögel-Knabner, I., & Han, X. (2011), Steppe ecosystems and climate and
855 land-use changes—vulnerability, feedbacks and possibilities for adaptation. *Plant and*
856 *Soil*, 340(1-2), 1-6. <https://doi.org/10.1007/s11104-010-0651-4>.

857 Butterworth, B. J., Desai, A. R., Townsend, P. A., Petty, G. W., Andresen, C. G., Bertram, T. H.,
858 et al. (2021), Connecting Land–Atmosphere Interactions to Surface Heterogeneity in
859 CHEESEHEAD19. *Bulletin of the American Meteorological Society*, 102(2), E421-E445.
860 <https://doi.org/10.1175/bams-d-19-0346.1>.

861 Charuchittipan, D., Babel, W., Mauder, M., Leps, J. P., & Foken, T. (2014), Extension of the
862 Averaging Time in Eddy-Covariance Measurements and Its Effect on the Energy Balance
863 Closure. *Boundary-Layer Meteorology*, 152(3), 303-327. [https://doi.org/10.1007/s10546-](https://doi.org/10.1007/s10546-014-9922-6)
864 [014-9922-6](https://doi.org/10.1007/s10546-014-9922-6).

865 Couvreux, F., Guichard, F., Masson, V., & Redelsperger, J. L. (2006), Negative water vapour
866 skewness and dry tongues in the convective boundary layer: observations and large-eddy
867 simulation budget analysis. *Boundary-Layer Meteorology*, 123(2), 269-294.
868 <https://doi.org/10.1007/s10546-006-9140-y>.

869 Couvreux, F., Guichard, F., Redelsperger, J. L., Kiemle, C., Masson, V., Lafore, J. P., & Flamant,
870 C. (2005), Water-vapour variability within a convective boundary-layer assessed by
871 large-eddy simulations and IHOP_2002 observations. *Quarterly Journal of the Royal*
872 *Meteorological Society*, 131(611), 2665-2693. <https://doi.org/10.1256/qj.04.167>.

873 Davis, K. J., Bakwin, P. S., Yi, C., Berger, B. W., Zhao, C., Teclaw, R. M., & Isebrands, J. G.
874 (2003), The annual cycles of CO₂ and H₂O exchange over a northern mixed forest as
875 observed from a very tall tower. *Global Change Biology*, 9(9), 1278-1293.
876 <https://doi.org/10.1046/j.1365-2486.2003.00672.x>.

877 Desai, A. (2023). *AmeriFlux BASE US-PFa Park Falls/WLEF*.
878 <https://doi.org/https://doi.org/10.17190/AMF/1246090>.

879 Desai, A. R., Bolstad, P. V., Cook, B. D., Davis, K. J., & Carey, E. V. (2005), Comparing net
880 ecosystem exchange of carbon dioxide between an old-growth and mature forest in the
881 upper Midwest, USA. *Agricultural and Forest Meteorology*, 128(1-2), 33-55.
882 <https://doi.org/10.1016/j.agrformet.2004.09.005>.

883 Desai, A. R., Murphy, B. A., Wiesner, S., Thom, J., Butterworth, B. J., Koupaei-Abyazani, N., et
884 al. (2022a), Drivers of Decadal Carbon Fluxes Across Temperate Ecosystems. *Journal of*
885 *Geophysical Research: Biogeosciences*, 127(12). <https://doi.org/10.1029/2022jg007014>.

886 Desai, A. R., Paleri, S., Mineau, J., Kadum, H., Wanner, L., Mauder, M., et al. (2022b), Scaling
887 Land-Atmosphere Interactions: Special or Fundamental? *Journal of Geophysical*
888 *Research: Biogeosciences*, 127(10). <https://doi.org/10.1029/2022jg007097>.

889 Desjardins, R. L., MacPherson, J. I., Mahrt, L., Schuepp, P., Pattey, E., Neumann, H., et al.
890 (1997), Scaling up flux measurements for the boreal forest using aircraft-tower
891 combinations. *Journal of Geophysical Research: Atmospheres*, 102(D24), 29125-29133.
892 <https://doi.org/10.1029/97jd00278>.

893 Desjardins, R. L., Macpherson, J. I., Neumann, H., Den Hartog, G., & Schuepp, P. H. (1995),
894 Flux estimates of latent and sensible heat, carbon dioxide, and ozone using an aircraft-
895 tower combination. *Atmospheric Environment*, 29(21), 3147-3158.
896 [https://doi.org/10.1016/1352-2310\(95\)00007-1](https://doi.org/10.1016/1352-2310(95)00007-1).

897 Dewitz, J., & U.S. Geological Survey. (2021). *National Land Cover Database (NLCD) 2019*
898 *Products*. <https://doi.org/doi:10.5066/P9KZCM54>.

899 Dowell, D. C., Alexander, C. R., James, E. P., Weygandt, S. S., Benjamin, S. G., Manikin, G. S.,
900 et al. (2022), The High-Resolution Rapid Refresh (HRRR): An Hourly Updating
901 Convection-Allowing Forecast Model. Part I: Motivation and System Description.
902 *Weather and Forecasting*, 37(8), 1371-1395. <https://doi.org/10.1175/Waf-D-21-0151.1>.

903 Eder, F., Schmidt, M., Damian, T., Träumner, K., & Mauder, M. (2015), Mesoscale Eddies
904 Affect Near-Surface Turbulent Exchange: Evidence from Lidar and Tower
905 Measurements. *Journal of Applied Meteorology and Climatology*, 54(1), 189-206.
906 <https://doi.org/10.1175/jamc-d-14-0140.1>.

907 Farge, M. (1992), Wavelet Transforms and Their Applications to Turbulence. *Annual Review of*
908 *Fluid Mechanics*, 24, 395-457. <https://doi.org/DOI 10.1146/annurev.fl.24.010192.002143>.

909 Finnigan, J. J., Clement, R., Malhi, Y., Leuning, R., & Cleugh, H. A. (2003), A Re-Evaluation of
910 Long-Term Flux Measurement Techniques Part I: Averaging and Coordinate Rotation.
911 *Boundary-Layer Meteorology*, 107(1), 1-48. <https://doi.org/10.1023/A:1021554900225>.

912 Foken, T., Aubinet, M., Finnigan, J. J., Leclerc, M. Y., Mauder, M., & Paw U, K. T. (2011),
913 Results Of A Panel Discussion About The Energy Balance Closure Correction For Trace

914 Gases. *Bulletin of the American Meteorological Society*, 92(4), ES13-ES18.
915 <https://doi.org/10.1175/2011bams3130.1>.

916 Foken, T., & Wichura, B. (1996), Tools for quality assessment of surface-based flux
917 measurements. *Agricultural and Forest Meteorology*, 78(1-2), 83-105. [https://doi.org/10.1016/0168-1923\(95\)02248-1](https://doi.org/10.1016/0168-1923(95)02248-1).
918

919 French, J., Oolman, L., & Plummer, D. (2021). *University of Wyoming King Air (UWKA) High*
920 *Rate Flight Level Data*. <https://doi.org/10.26023/5B70-4VP5-XY0V>.

921 Gao, Z. M., Liu, H. P., Russell, E. S., Huang, J. P., Foken, T., & Oncley, S. P. (2016), Large
922 eddies modulating flux convergence and divergence in a disturbed unstable atmospheric
923 surface layer. *Journal of Geophysical Research-Atmospheres*, 121(4), 1475-1492.
924 <https://doi.org/10.1002/2015jd024529>.

925 Garratt, J. (1994), Review: the atmospheric boundary layer. *Earth-Science Reviews*, 37(1-2), 89-
926 134. [https://doi.org/10.1016/0012-8252\(94\)90026-4](https://doi.org/10.1016/0012-8252(94)90026-4).

927 Haimov, S., & Rodi, A. (2013), Fixed-Antenna Pointing-Angle Calibration of Airborne Doppler
928 Cloud Radar. *Journal of Atmospheric and Oceanic Technology*, 30(10), 2320-2335.
929 <https://doi.org/10.1175/Jtech-D-12-00262.1>.

930 Halldin, S., Gryning, S. E., Gottschalk, L., Jochum, A., Lundin, L. C., & Van de Griend, A. A.
931 (1999), Energy, water and carbon exchange in a boreal forest landscape — NOPEX
932 experiences. *Agricultural and Forest Meteorology*, 98-99, 5-29.
933 [https://doi.org/10.1016/s0168-1923\(99\)00148-3](https://doi.org/10.1016/s0168-1923(99)00148-3).

934 Helbig, M., Gerken, T., Beamesderfer, E. R., Baldocchi, D. D., Banerjee, T., Biraud, S. C., et al.
935 (2021), Integrating continuous atmospheric boundary layer and tower-based flux
936 measurements to advance understanding of land-atmosphere interactions. *Agricultural*
937 *and Forest Meteorology*, 307. <https://doi.org/10.1016/j.agrformet.2021.108509>.

938 Hill, T. C., Williams, M., & Moncrieff, J. B. (2008), Modeling feedbacks between a boreal forest
939 and the planetary boundary layer. *Journal of Geophysical Research*, 113(D15).
940 <https://doi.org/10.1029/2007jd009412>.

941 Hill, T. C., Williams, M., Woodward, F. I., & Moncrieff, J. B. (2011), Constraining ecosystem
942 processes from tower fluxes and atmospheric profiles. *Ecol Appl*, 21(5), 1474-1489.
943 <https://doi.org/10.1890/09-0840.1>.

944 Hu, X. M., Gourdjji, S. M., Davis, K. J., Wang, Q., Zhang, Y., Xue, M., et al. (2021),
945 Implementation of Improved Parameterization of Terrestrial Flux in WRF-VPRM
946 Improves the Simulation of Nighttime CO₂ Peaks and a Daytime CO₂ Band Ahead of a
947 Cold Front. *Journal of Geophysical Research: Atmospheres*, 126(10).
948 <https://doi.org/10.1029/2020jd034362>.

949 Hu, X. M., Huang, Y., Xue, M., Martin, E., Hong, Y., Chen, M., et al. (2023), Effects of Lower
950 Troposphere Vertical Mixing on Simulated Clouds and Precipitation Over the Amazon
951 During the Wet Season. *Journal of Geophysical Research: Atmospheres*, 128(12).
952 <https://doi.org/10.1029/2023jd038553>.

953 Kiemle, C., Brewer, W. A., Ehret, G., Hardesty, R. M., Fix, A., Senff, C., et al. (2007), Latent
954 Heat Flux Profiles from Collocated Airborne Water Vapor and Wind Lidars during
955 IHOP_2002. *Journal of Atmospheric and Oceanic Technology*, 24(4), 627-639.
956 <https://doi.org/10.1175/jtech1997.1>.

957 LeMone, M. A., Angevine, W. M., Bretherton, C. S., Chen, F., Dudhia, J., Fedorovich, E., et al.
958 (2019), 100 Years of Progress in Boundary Layer Meteorology. *Meteorological*
959 *Monographs*, 59, 9.1-9.85. <https://doi.org/10.1175/amsmonographs-d-18-0013.1>.

960 Lin, G., Geerts, B., Wang, Z. E., Grasmick, C., Jing, X. Q., & Yang, J. (2019), Interactions
961 between a Nocturnal MCS and the Stable Boundary Layer as Observed by an Airborne
962 Compact Raman Lidar during PECAN. *Monthly Weather Review*, 147(9), 3169-3189.
963 <https://doi.org/10.1175/Mwr-D-18-0388.1>.

964 Lin, G., Grasmick, C., Geerts, B., Wang, Z. E., & Deng, M. (2021), Convection Initiation and
965 Bore Formation Following the Collision of Mesoscale Boundaries over a Developing
966 Stable Boundary Layer: A Case Study from PECAN. *Monthly Weather Review*, 149(7),
967 2351-2367. <https://doi.org/10.1175/Mwr-D-20-0282.1>.

968 Lin, G., Wang, Z., Ziegler, C., Hu, X.-M., Xue, M., Geerts, B., & Chu, Y. (2023), A Comparison
969 of Convective Storm Inflow Moisture Variability between the Great Plains and the
970 Southeastern United States Using Multiplatform Field Campaign Observations. *Journal*
971 *of Atmospheric and Oceanic Technology*, 40(5), 539-556. [https://doi.org/10.1175/jtech-d-](https://doi.org/10.1175/jtech-d-22-0037.1)
972 [22-0037.1](https://doi.org/10.1175/jtech-d-22-0037.1).

973 Linné, H., Hennemuth, B., Bösenberg, J., & Ertel, K. (2006), Water vapour flux profiles in the
974 convective boundary layer. *Theoretical and Applied Climatology*, 87(1-4), 201-211.
975 <https://doi.org/10.1007/s00704-005-0191-7>.

976 Liu, B., Wang, Z., Cai, Y., Wechsler, P., Kuestner, W., Burkhardt, M., & Welch, W. (2014),
977 Compact airborne Raman lidar for profiling aerosol, water vapor and clouds. *Opt Express*,
978 22(17), 20613-20621. <https://doi.org/10.1364/OE.22.020613>.

979 Mahrt, L. (1998), Flux sampling errors for aircraft and towers. *Journal of Atmospheric and*
980 *Oceanic Technology*, 15(2), 416-429. [https://doi.org/10.1175/1520-0426\(1998\)015<0416:Fsefaa>2.0.Co;2](https://doi.org/10.1175/1520-0426(1998)015<0416:Fsefaa>2.0.Co;2).

982 Mahrt, L. (2000), Surface Heterogeneity and Vertical Structure of the Boundary Layer.
983 *Boundary-Layer Meteorology*, 96(1-2), 33-62. <https://doi.org/10.1023/a:1002482332477>.

984 Mahrt, L. (2010), Computing turbulent fluxes near the surface: Needed improvements.
985 *Agricultural and Forest Meteorology*, 150(4), 501-509.
986 <https://doi.org/10.1016/j.agrformet.2010.01.015>.

987 Margairaz, F., Pardyjak, E. R., & Calaf, M. (2020), Surface Thermal Heterogeneities and the
988 Atmospheric Boundary Layer: The Relevance of Dispersive Fluxes. *Boundary-Layer*
989 *Meteorology*, 175(3), 369-395. <https://doi.org/10.1007/s10546-020-00509-w>.

990 Mauder, M., Desjardins, R. L., & MacPherson, I. (2007), Scale analysis of airborne flux
991 measurements over heterogeneous terrain in a boreal ecosystem. *Journal of Geophysical*
992 *Research: Atmospheres*, 112(D13). <https://doi.org/10.1029/2006jd008133>.

993 Mauder, M., Foken, T., & Cuxart, J. (2020), Surface-Energy-Balance Closure over Land: A
994 Review. *Boundary-Layer Meteorology*, 177(2-3), 395-426.
995 <https://doi.org/10.1007/s10546-020-00529-6>.

996 Mauder, M., Jegede, O. O., Okogbue, E. C., Wimmer, F., & Foken, T. (2006), Surface energy
997 balance measurements at a tropical site in West Africa during the transition from dry to
998 wet season. *Theoretical and Applied Climatology*, 89(3-4), 171-183.
999 <https://doi.org/10.1007/s00704-006-0252-6>.

1000 Metzger, S., Durden, D., Paleri, S., Sühling, M., Butterworth, B. J., Florian, C., et al. (2021),
1001 Novel approach to observing system simulation experiments improves information gain
1002 of surface–atmosphere field measurements. *Atmospheric Measurement Techniques*,
1003 14(11), 6929-6954. <https://doi.org/10.5194/amt-14-6929-2021>.

1004 Metzger, S., Junkermann, W., Mauder, M., Butterbach-Bahl, K., Trancón y Widemann, B., Neidl,
1005 F., et al. (2013), Spatially explicit regionalization of airborne flux measurements using
1006 environmental response functions. *Biogeosciences*, 10(4), 2193-2217.
1007 <https://doi.org/10.5194/bg-10-2193-2013>.

1008 Oncley, S. (2021). *NCAR/EOL 5 minute ISFS surface flux data, tilt corrected, geographic*
1009 *coordinate winds*. <https://doi.org/https://doi.org/10.26023/43MF-NP8N-3Q0V>.

1010 Orlanski, I. (1975), A rational subdivision of scales for atmospheric processes. *Bulletin of the*
1011 *American Meteorological Society*, 56(5), 527-534.
1012 <https://doi.org/https://doi.org/10.1175/1520-0477-56.5.527>.

1013 Paleri, S., Desai, A. R., Metzger, S., Durden, D., Butterworth, B. J., Mauder, M., et al. (2022),
1014 Space-Scale Resolved Surface Fluxes Across a Heterogeneous, Mid-Latitude Forested
1015 Landscape. *Journal of Geophysical Research: Atmospheres*, 127(23).
1016 <https://doi.org/10.1029/2022jd037138>.

1017 Pielke, R. A., Sr, Avissar, R., Raupach, M., Dolman, A. J., Zeng, X., & Denning, A. S. (2003),
1018 Interactions between the atmosphere and terrestrial ecosystems: influence on weather and
1019 climate. *Global Change Biology*, 4(5), 461-475. [https://doi.org/10.1046/j.1365-](https://doi.org/10.1046/j.1365-2486.1998.t01-1-00176.x)
1020 [2486.1998.t01-1-00176.x](https://doi.org/10.1046/j.1365-2486.1998.t01-1-00176.x).

1021 Platis, A., Moene, A. F., Villagrasa, D. M., Beyrich, F., Tupman, D., & Bange, J. (2017),
1022 Observations of the Temperature and Humidity Structure Parameter Over Heterogeneous
1023 Terrain by Airborne Measurements During the LITFASS-2003 Campaign. *Boundary-*
1024 *Layer Meteorology*, 165(3), 447-473. <https://doi.org/10.1007/s10546-017-0290-x>.

1025 Pressel, K. G., Collins, W. D., & Desai, A. R. (2014), The spatial scale dependence of water
1026 vapor variability inferred from observations from a very tall tower. *Journal of*
1027 *Geophysical Research: Atmospheres*, 119(16), 9822-9837.
1028 <https://doi.org/10.1002/2013jd021141>.

1029 Raupach, M. R., & Finnigan, J. J. (1995), Scale Issues in Boundary-Layer Meteorology -
1030 Surface-Energy Balances in Heterogeneous Terrain. *Hydrological Processes*, 9(5-6),
1031 589-612. <https://doi.org/DOI 10.1002/hyp.3360090509>.

1032 Sellers, P., Hall, F., Ranson, K. J., Margolis, H., Kelly, B., Baldocchi, D., et al. (1995), The
1033 Boreal Ecosystem–Atmosphere Study (BOREAS): An Overview and Early Results from

1034 the 1994 Field Year. *Bulletin of the American Meteorological Society*, 76(9), 1549-1577.
1035 [https://doi.org/10.1175/1520-0477\(1995\)076<1549:Tbesao>2.0.Co;2](https://doi.org/10.1175/1520-0477(1995)076<1549:Tbesao>2.0.Co;2).

1036 Steinfeld, G., Letzel, M. O., Raasch, S., Kanda, M., & Inagaki, A. (2007), Spatial
1037 representativeness of single tower measurements and the imbalance problem with eddy-
1038 covariance fluxes: results of a large-eddy simulation study. *Boundary-Layer Meteorology*,
1039 123(1), 77-98. <https://doi.org/10.1007/s10546-006-9133-x>.

1040 Stevens, B., & Bony, S. (2013), Water in the atmosphere. *Physics Today*, 66(6), 29-34.
1041 <https://doi.org/10.1063/pt.3.2009>.

1042 Strunin, M. A., & Hiyama, T. (2005), Spectral Structure of Small-Scale Turbulent and Mesoscale
1043 Fluxes in the Atmospheric Boundary Layer over a Thermally Inhomogeneous Land
1044 Surface. *Boundary-Layer Meteorology*, 117(3), 479-510. [https://doi.org/10.1007/s10546-](https://doi.org/10.1007/s10546-005-2188-2)
1045 [005-2188-2](https://doi.org/10.1007/s10546-005-2188-2).

1046 Stull, R. (1988). *An introduction to boundary layer meteorology* (Vol. Vol.13): Springer Science
1047 & Business Media.

1048 Stull, R. B. (2015), *Practical Meteorology-An Algebra-based Survey of Atmospheric Science*.
1049 *University of British Columbia*.

1050 Sun, X.-M., Zhu, Z.-L., Wen, X.-F., Yuan, G.-F., & Yu, G.-R. (2006), The impact of averaging
1051 period on eddy fluxes observed at ChinaFLUX sites. *Agricultural and Forest*
1052 *Meteorology*, 137(3-4), 188-193. <https://doi.org/10.1016/j.agrformet.2006.02.012>.

1053 Sun, Y., Jia, L., Chen, Q., Lin, X., Sude, B., Quan, Z., & Hutjes, R. W. A. (2023), Construction
1054 of a spatially gridded heat flux map based on airborne flux Measurements using remote
1055 sensing and machine learning methods. *Agricultural and Forest Meteorology*, 334.
1056 <https://doi.org/10.1016/j.agrformet.2023.109424>.

1057 Thomas, C., & Foken, T. (2004), Detection of long-term coherent exchange over spruce forest
1058 using wavelet analysis. *Theoretical and Applied Climatology*, 80(2-4), 91-104.
1059 <https://doi.org/10.1007/s00704-004-0093-0>.

1060 Torrence, C., & Compo, G. P. (1998), A Practical Guide to Wavelet Analysis. *Bulletin of the*
1061 *American Meteorological Society*, 79(1), 61-78. [https://doi.org/10.1175/1520-](https://doi.org/10.1175/1520-0477(1998)079<0061:Apgtwa>2.0.Co;2)
1062 [0477\(1998\)079<0061:Apgtwa>2.0.Co;2](https://doi.org/10.1175/1520-0477(1998)079<0061:Apgtwa>2.0.Co;2).

- 1063 Vadrevu, K. P., & Choi, Y. (2011), Wavelet analysis of airborne CO₂ measurements and related
1064 meteorological parameters over heterogeneous landscapes. *Atmospheric Research*, 102(1-
1065 2), 77-90. <https://doi.org/10.1016/j.atmosres.2011.06.008>.
- 1066 Wang, Z., Wechsler, P., Kuestner, W., French, J., Rodi, A., Glover, B., et al. (2009), Wyoming
1067 Cloud Lidar: instrument description and applications. *Optics Express*, 17(16), 13576-
1068 13587. <https://doi.org/10.1364/OE.17.013576>.
- 1069 Wolf, B., Chwala, C., Fersch, B., Garvelmann, J., Junkermann, W., Zeeman, M. J., et al. (2017),
1070 The SCALEX Campaign: Scale-Crossing Land Surface and Boundary Layer Processes in
1071 the TERENO-preAlpine Observatory. *Bulletin of the American Meteorological Society*,
1072 98(6), 1217-1234. <https://doi.org/10.1175/bams-d-15-00277.1>.
- 1073 Wu, D., Wang, Z., Wechsler, P., Mahon, N., Deng, M., Glover, B., et al. (2016), Airborne
1074 compact rotational Raman lidar for temperature measurement. *Opt Express*, 24(18),
1075 A1210-1223. <https://doi.org/10.1364/OE.24.0A1210>.
- 1076

Figure 1.

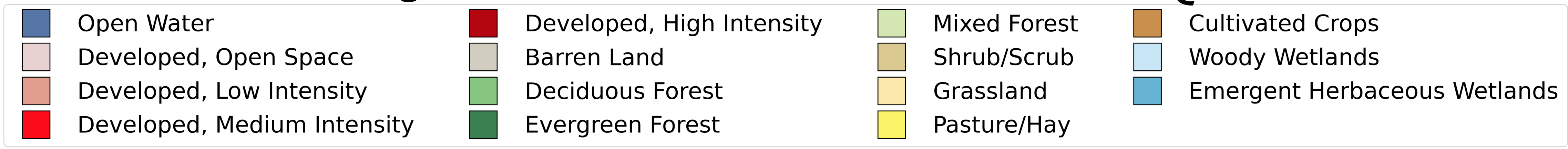
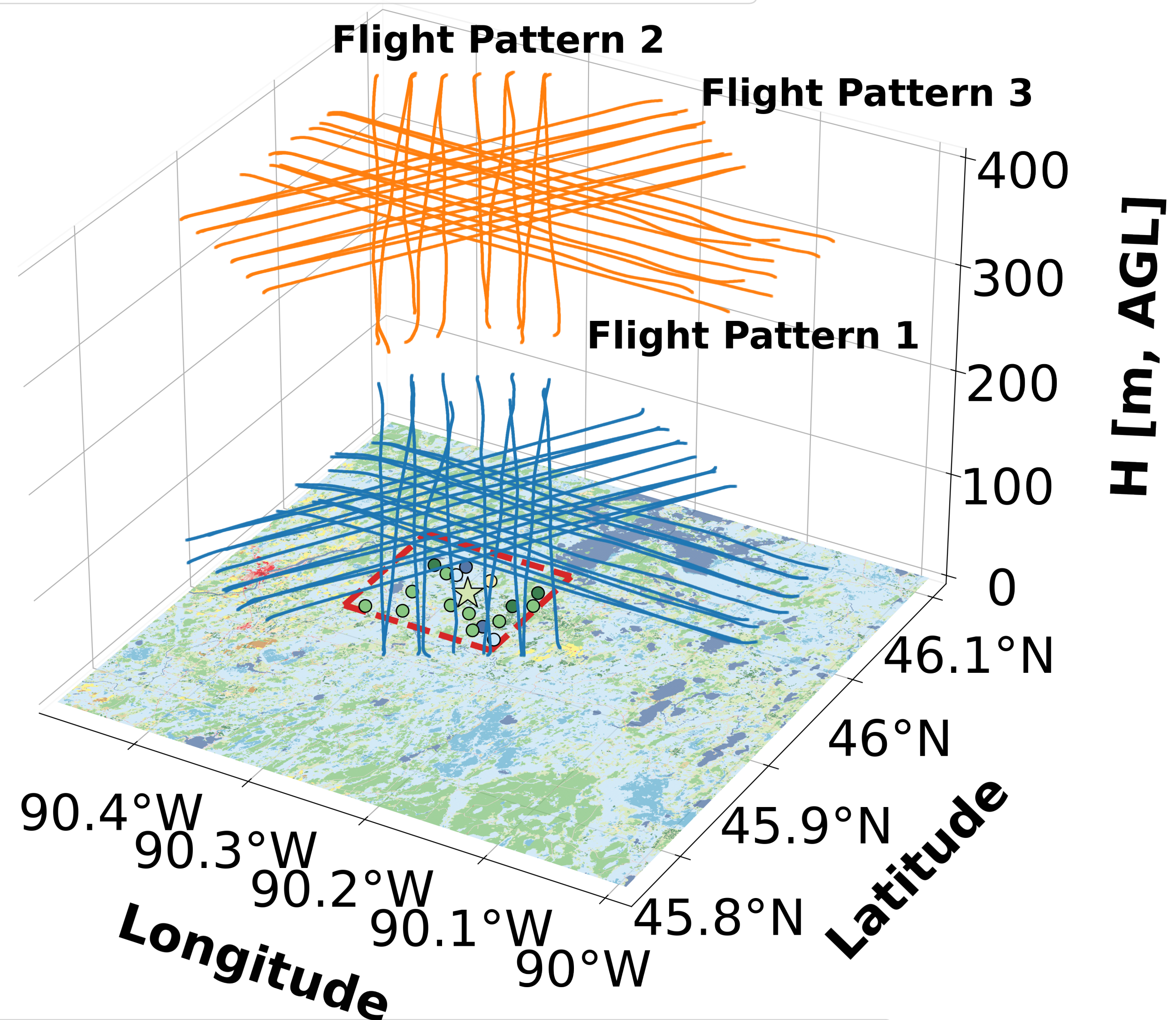
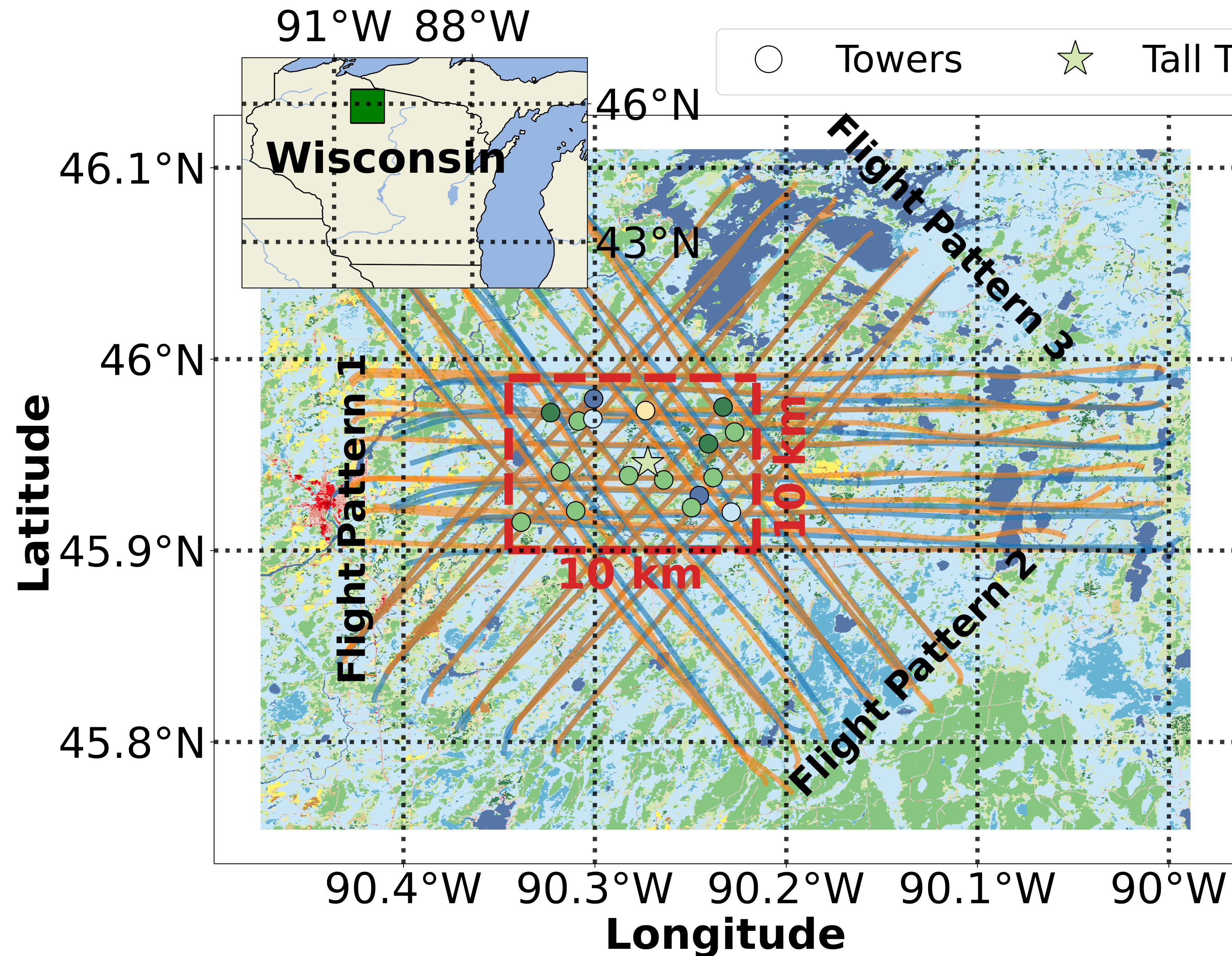


Figure 2.

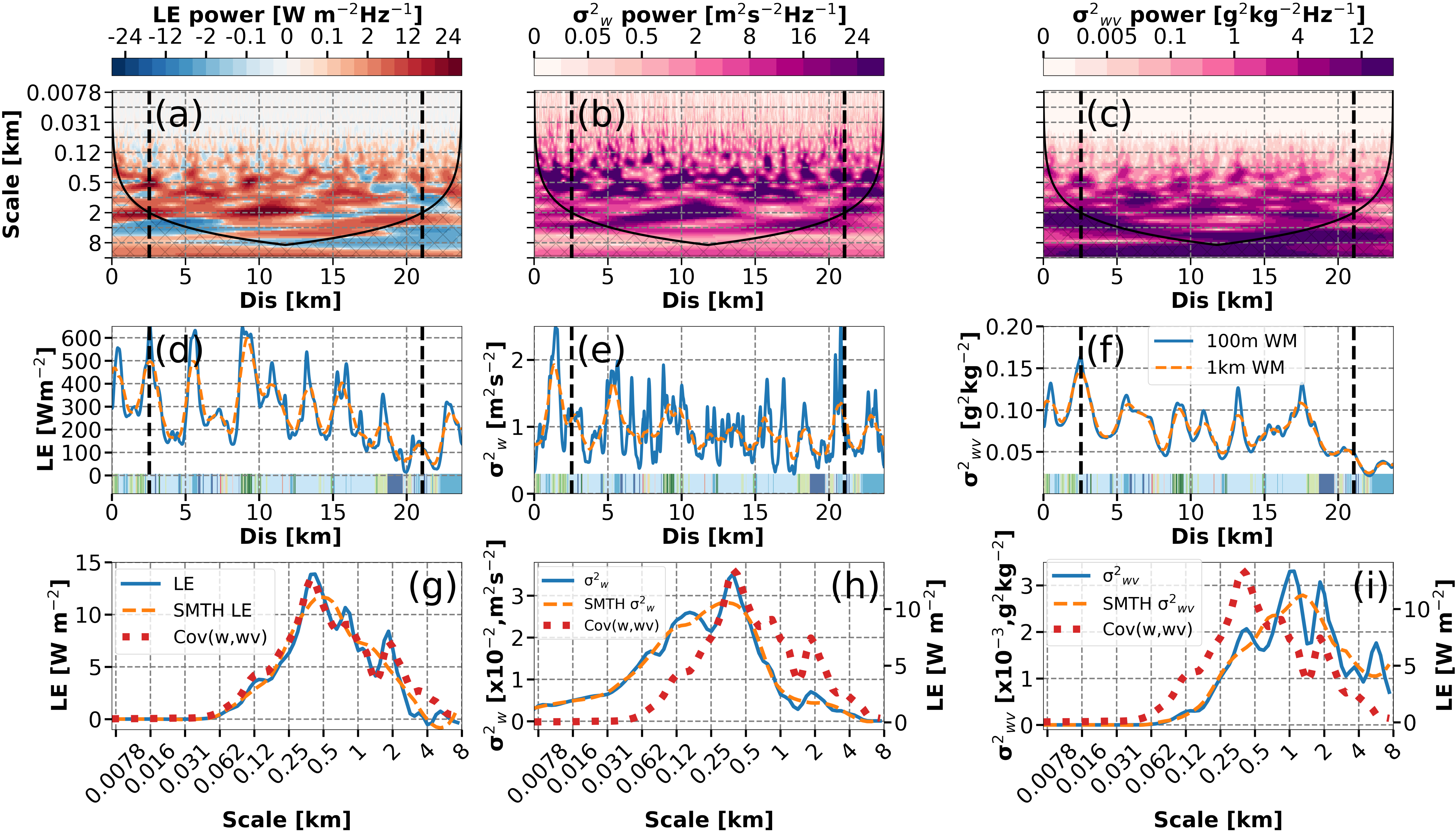


Figure 3.

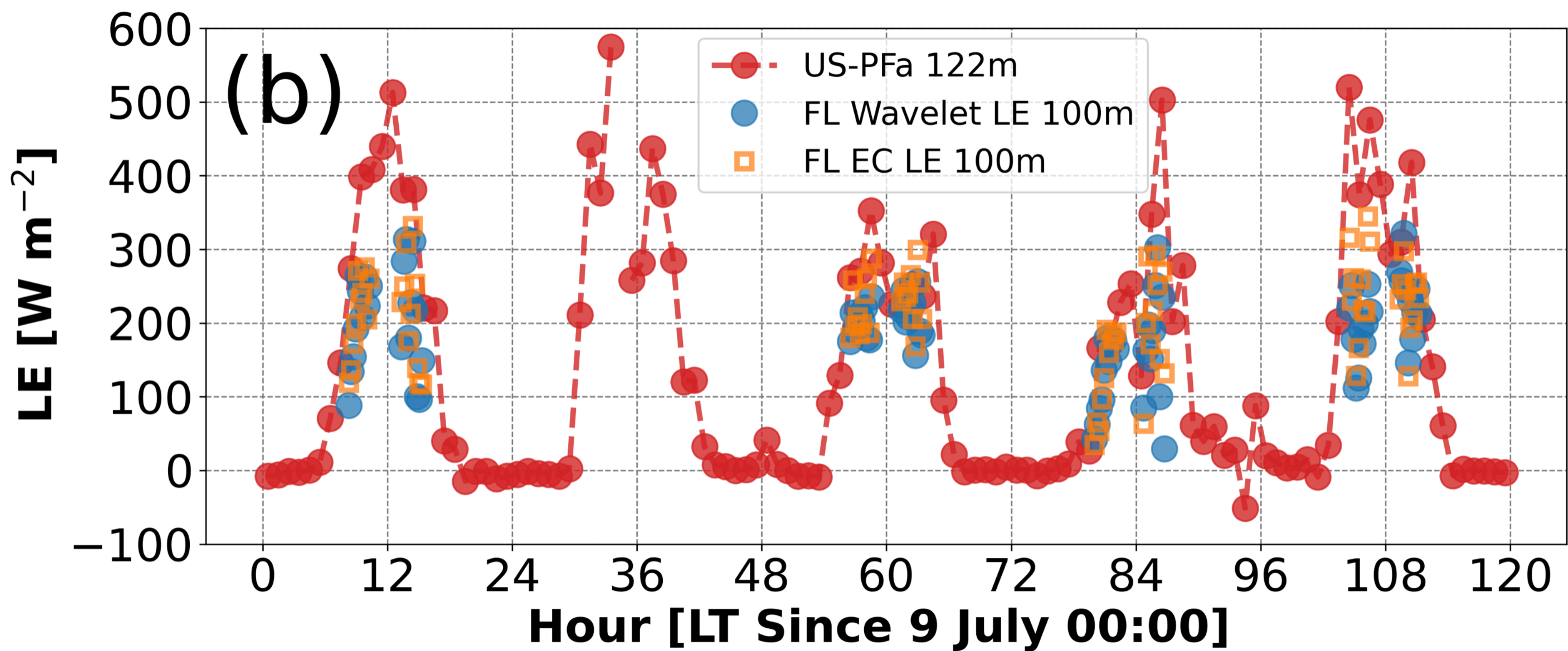
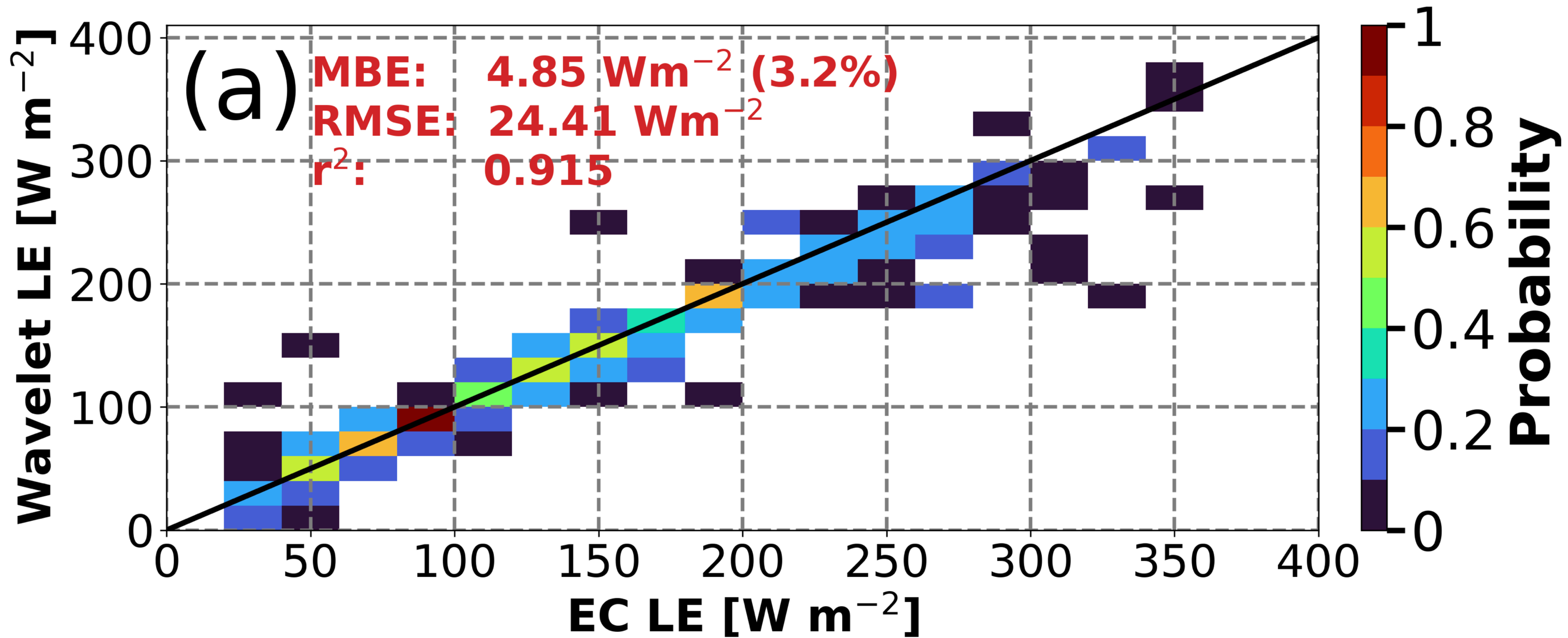


Figure 4.

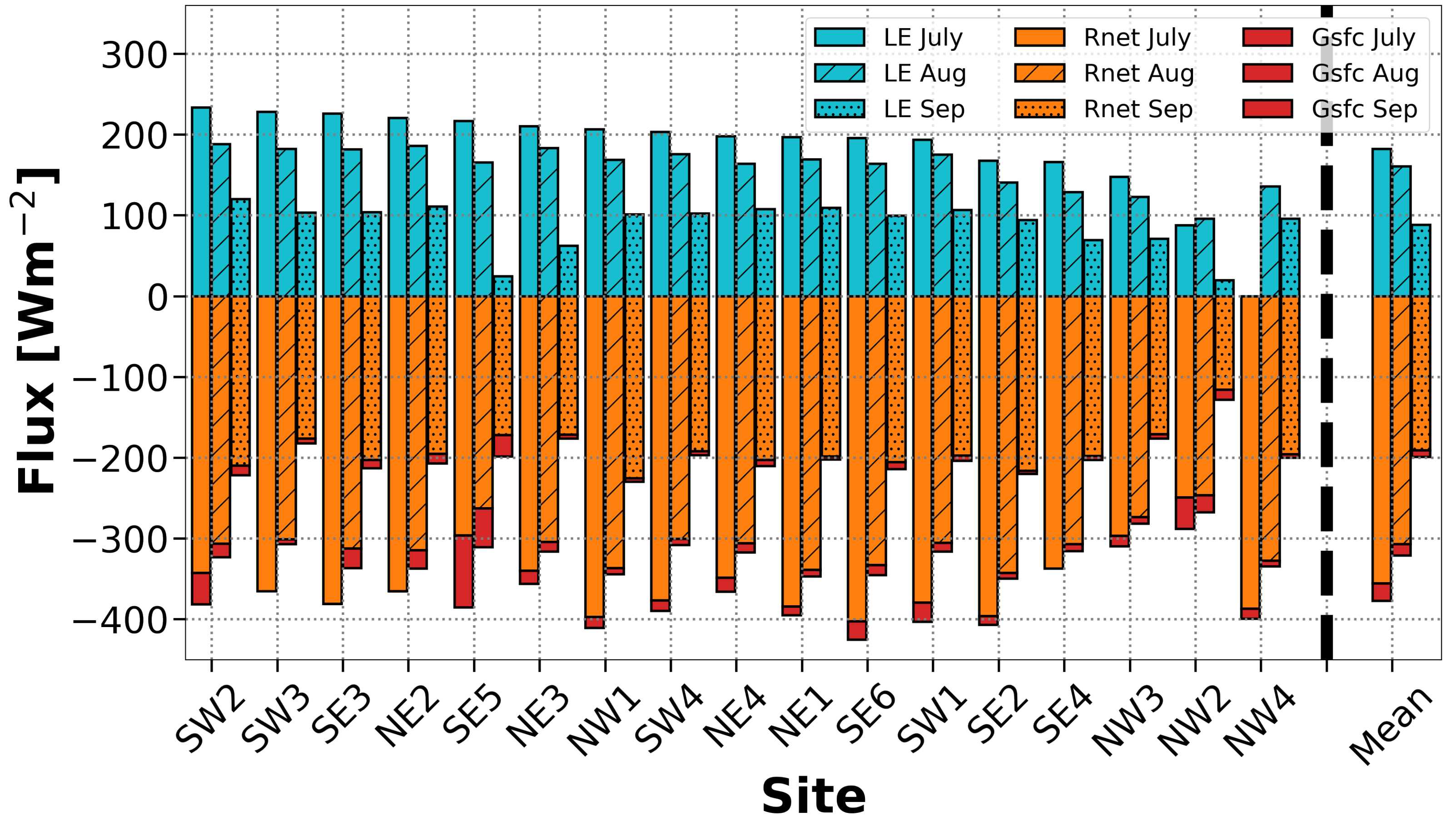


Figure 5.

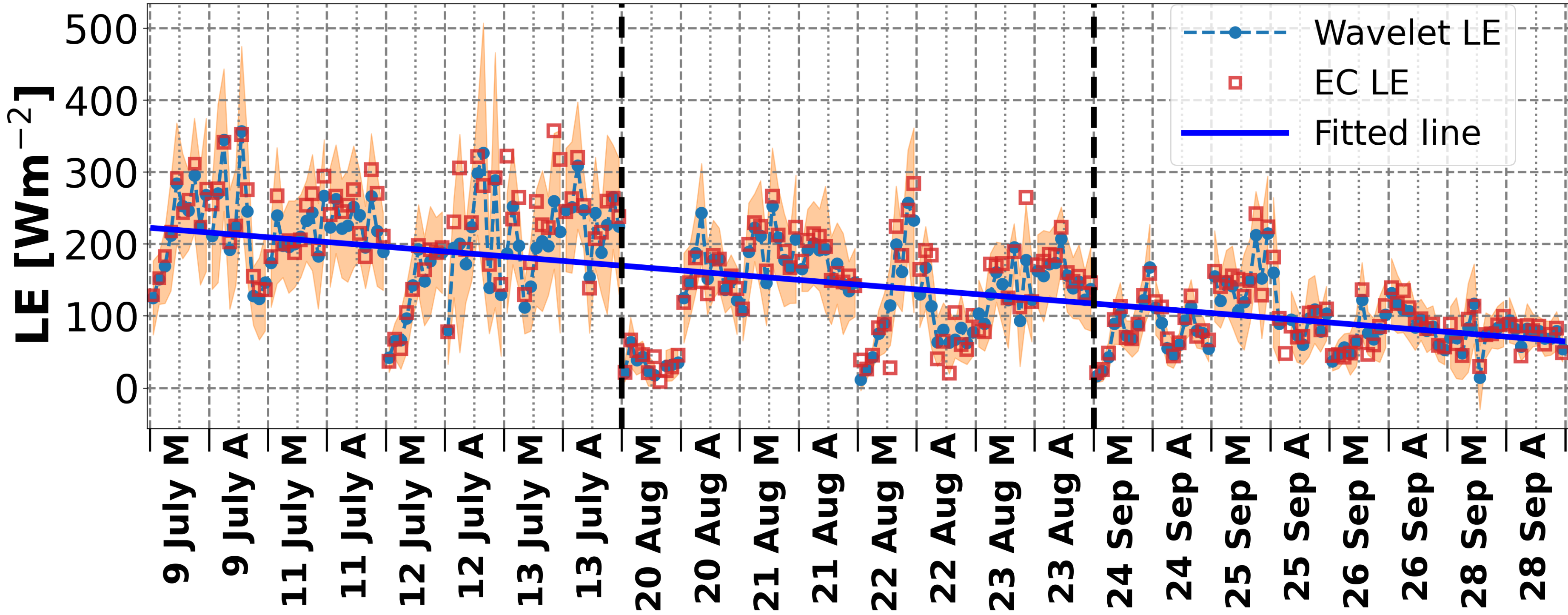


Figure 6.

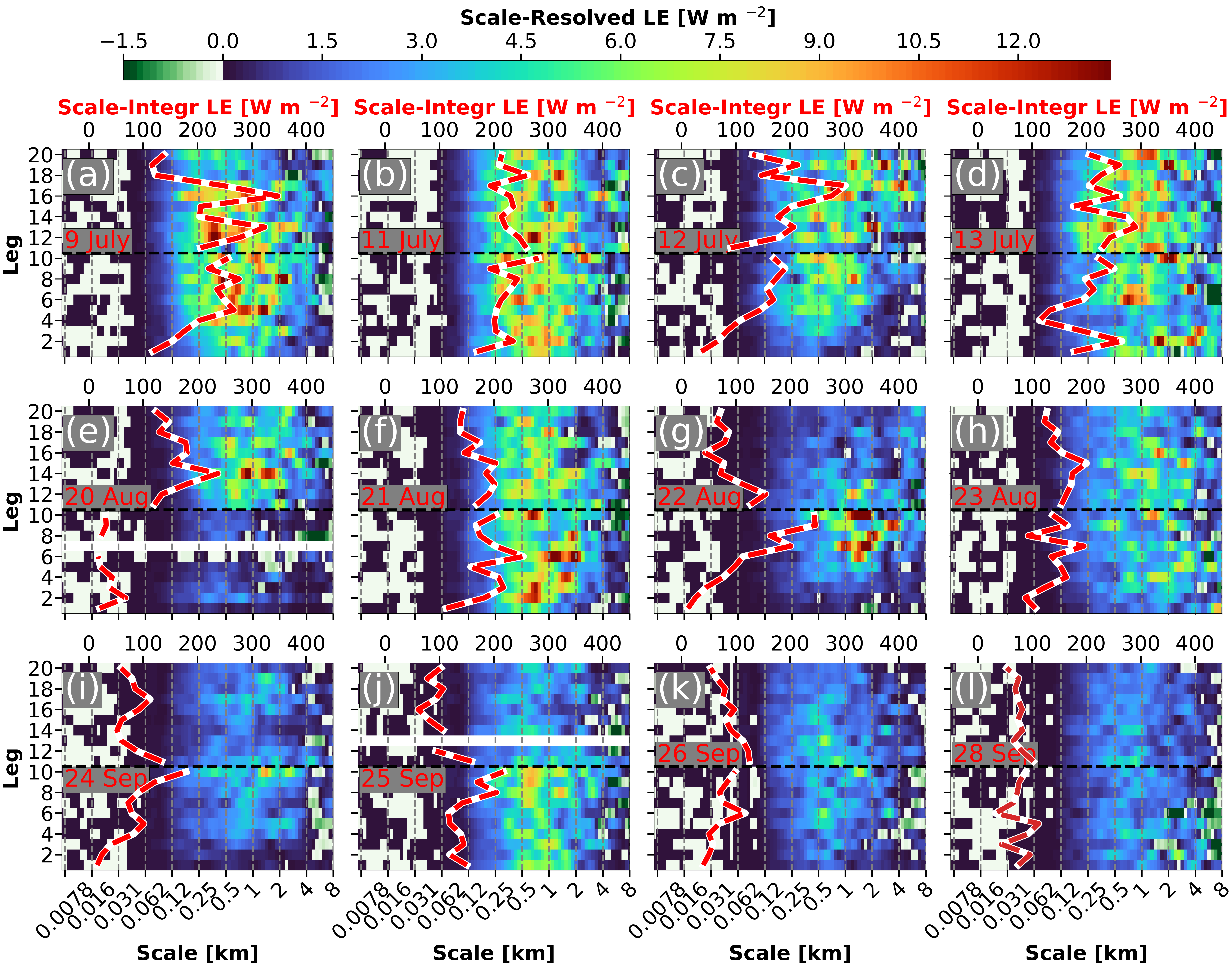


Figure 7.

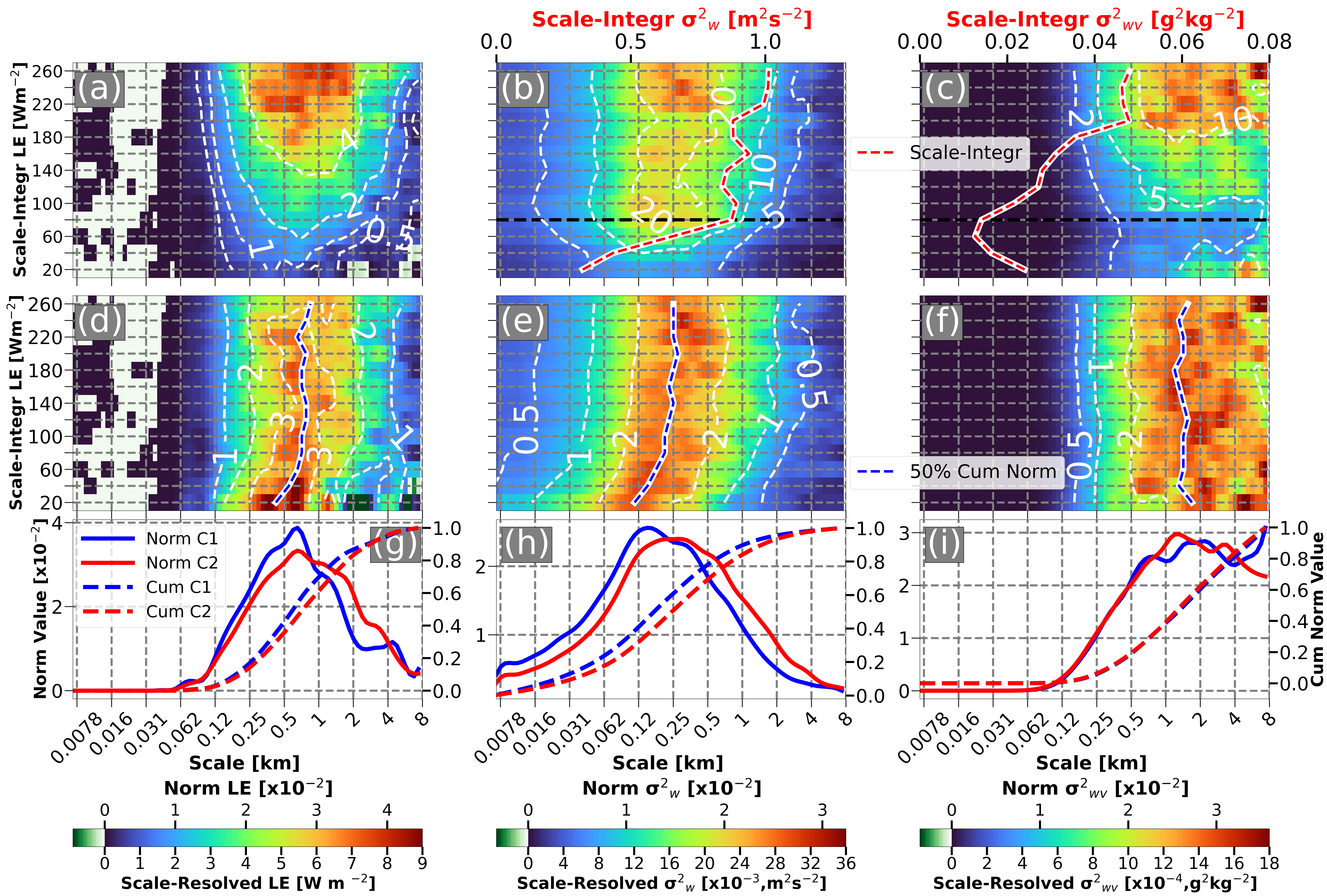


Figure 8.

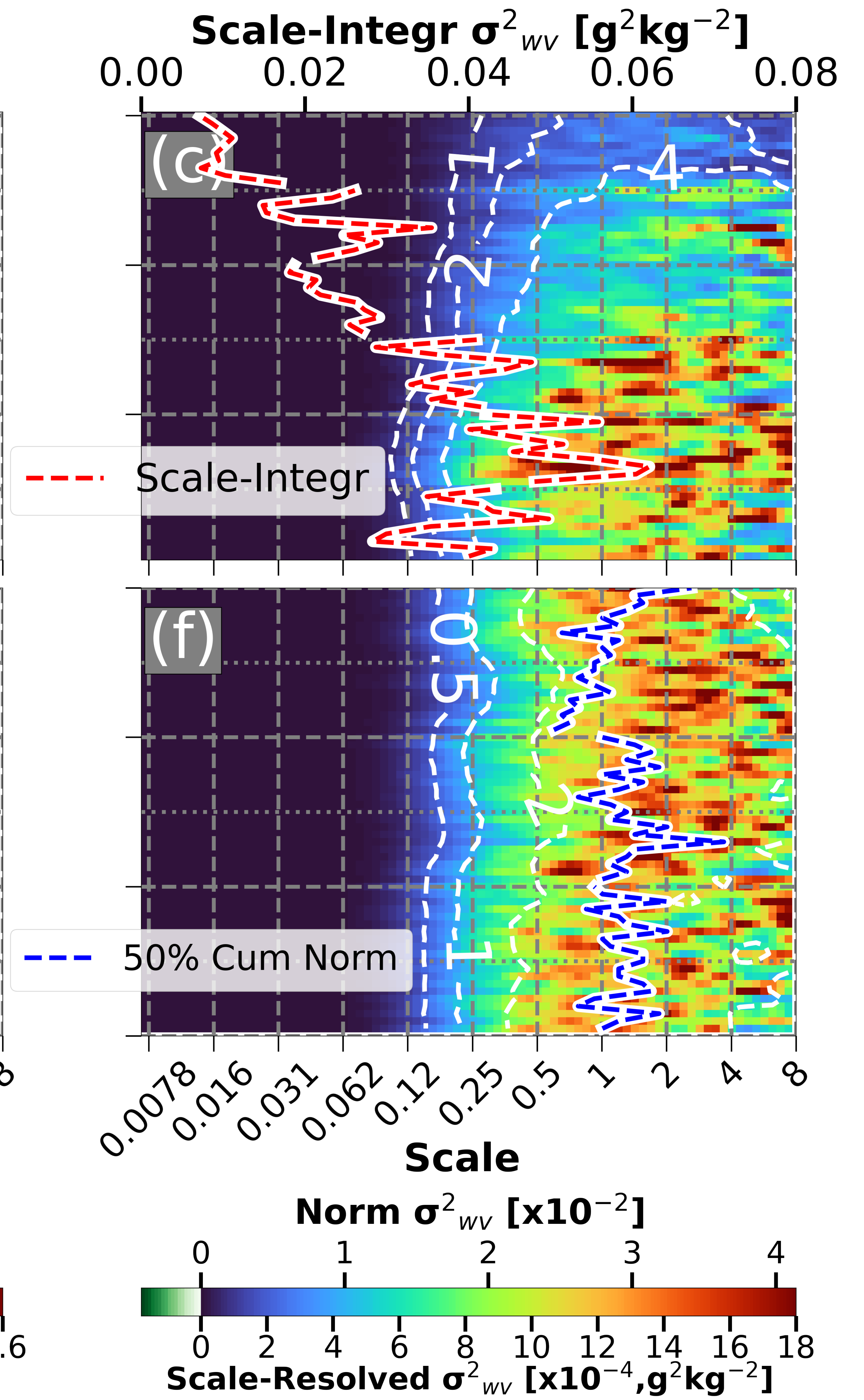
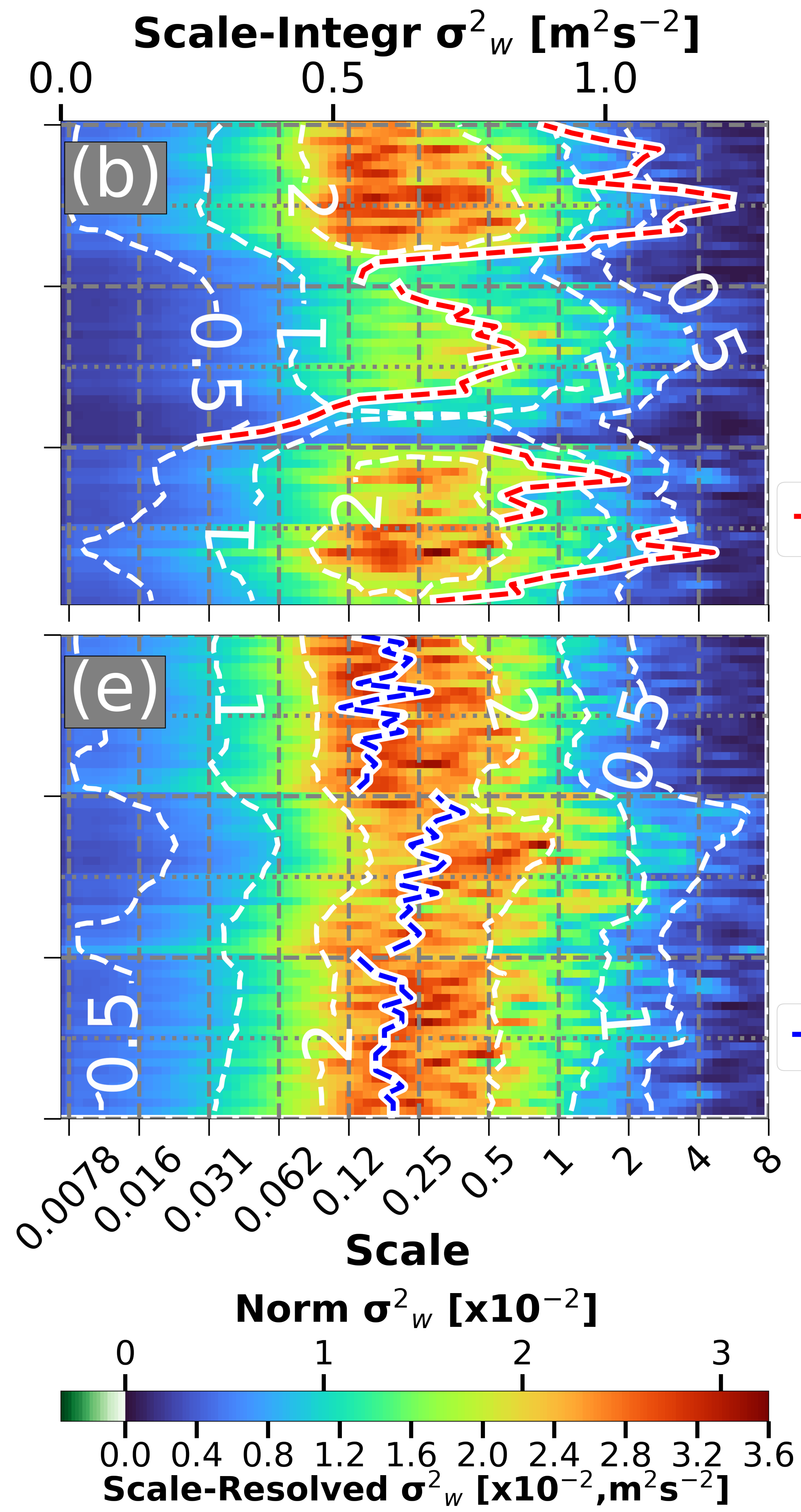
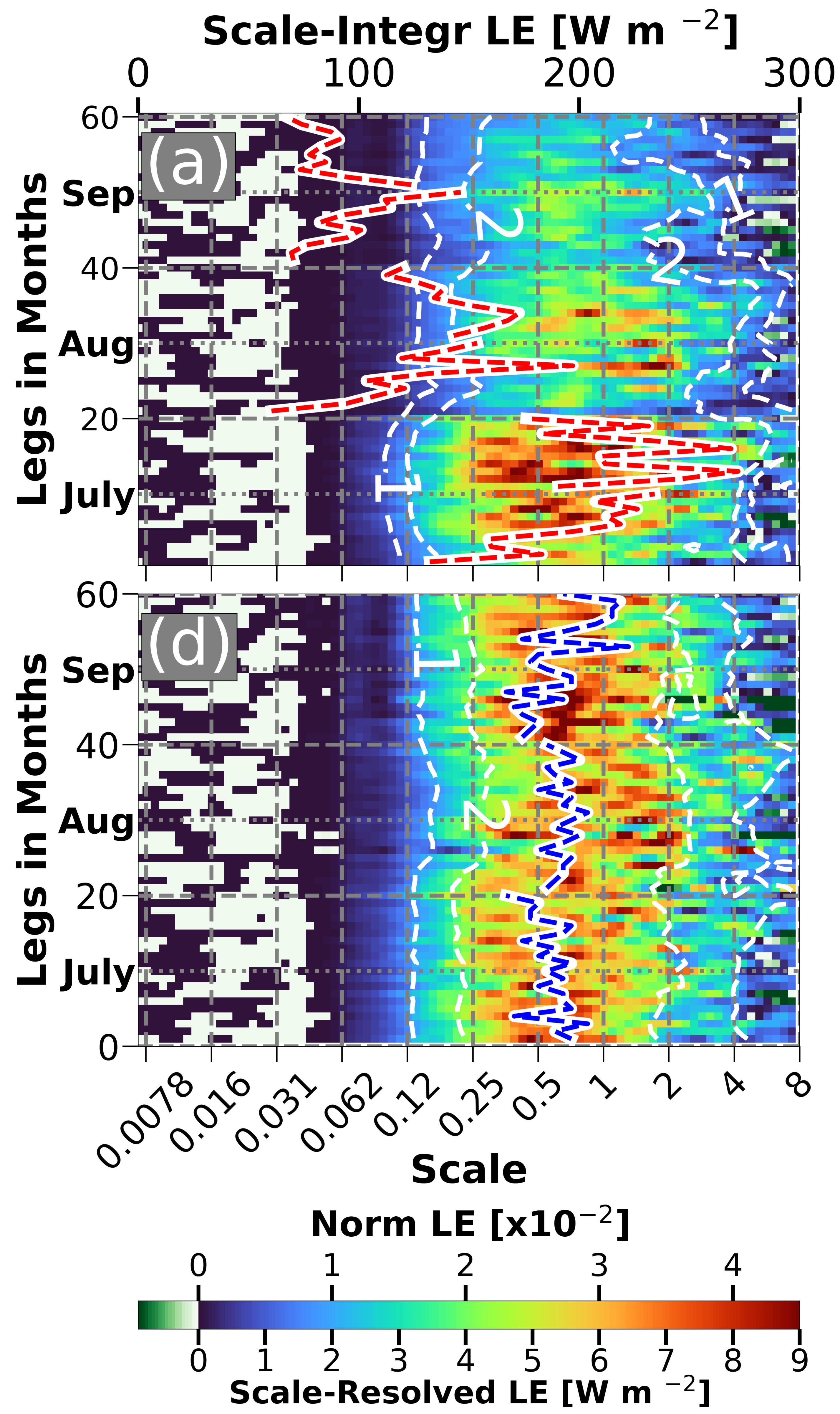


Figure 9.

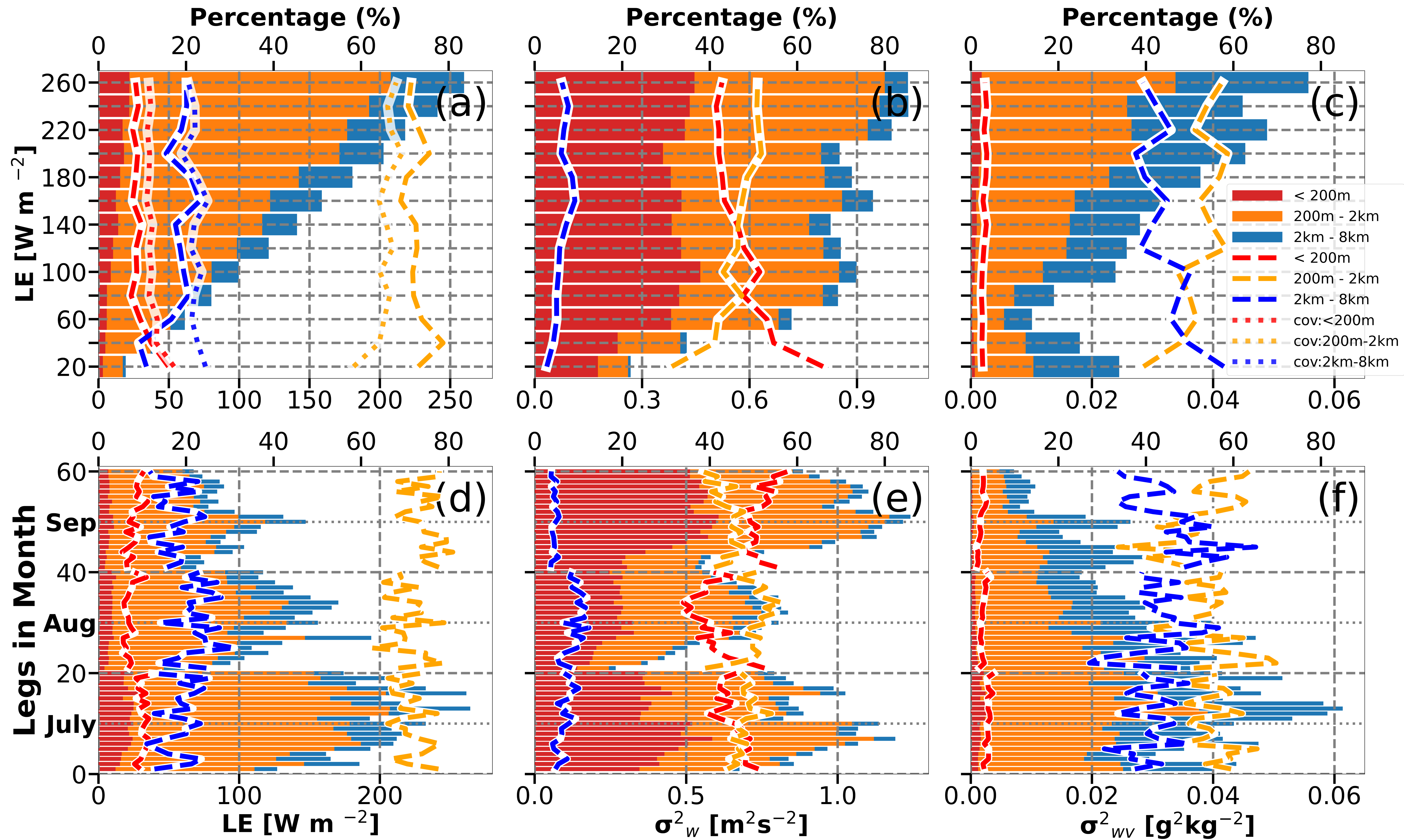


Figure 10.

